Journal of Geophysical Research: Atmospheres

RESEARCH ARTICLE
10.1029/2017JD028032

Special Section:
Quantifying the Emission, Properties, and Diverse Impacts of Wildfire Smoke

Photopolarimetric Sensitivity to Black Carbon Content of Wildfire Smoke: Results From the 2016 ImPACT-PM Field Campaign

O. V. Kalashnikova[1], M. J. Garay[1], K. H. Bates[2,3], C. M. Kenseth[2], W. Kong[2], C. D. Cappa[4], A. I. Lyapustin[5], H. H. Jonsson[6], F. C. Seidel[1], F. Xu[1], D. J. Diner[1], and J. H. Seinfeld[2]

[1]Jet Propulsion Laboratory, California Institute of Technology, Pasadena, CA, USA, [2]Department of Chemical Engineering, California Institute of Technology, Pasadena, CA, USA, [3]Now at Harvard University Center for the Environment, Cambridge, MA, USA, [4]Department of Civil and Environmental Engineering, University of California, Davis, CA, USA, [5]NASA Goddard Flight Space Center, Greenbelt, MD, USA, [6]CIRPAS, Naval Postgraduate School, Monterey, CA, USA

Key Points:
- Polarimetric observations are shown to be sensitive to the amount of black carbon in a wildfire smoke plume
- Radiative closure was achieved between multiangle polarimetric remote sensing and in situ airborne measurements in the smoke plume
- We demonstrated the ability of polarimetric data to constrain the black carbon mass fraction assuming external mixing of chemical components

Correspondence to:
O. V. Kalashnikova,
Olga.Kalashnikova@jpl.nasa.gov

Citation:
Kalashnikova, O. V., Garay, M. J., Bates, K. H., Kenseth, C. M., Kong, W., Cappa, C. D., et al. (2018). Photopolarimetric sensitivity to black carbon content of wildfire smoke: Results from the 2016 ImPACT-PM field campaign. *Journal of Geophysical Research: Atmospheres*, *123*, 5376–5396. https://doi.org/10.1029/2017JD028032

Received 8 NOV 2017
Accepted 8 APR 2018
Accepted article online 16 APR 2018
Published online 19 MAY 2018

Abstract Detailed characterization of the aerosol content of wildfire smoke plumes is typically performed through in situ aircraft observations, which have limited temporal and spatial coverage. Extending such observations to regional or global scales requires new remote sensing approaches, such as retrievals that make use of spectropolarimetric, multiangle imaging. In this work measurements made during the Imaging Polarimetric Assessment and Characterization of Tropospheric Particulate Matter (ImPACT-PM) field campaign in a smoke plume near the town of Lebec in Southern California by the Navy Center for Interdisciplinary Remotely Piloted Aircraft Studies Twin Otter aircraft on 8 July 2016 are used in conjunction with near-coincident measurements from the Airborne Multiangle SpectroPolarimetric Imager (AirMSPI) on the National Aeronautics and Space Administration ER-2 high-altitude research aircraft to assess the sensitivity of spectropolarimetric measurements to the black carbon content of the plume. Tracking visible features in the smoke through the sequence of AirMSPI observations allowed the height of the plume to be estimated through geometric techniques. Then, by constraining the fractional amounts of the aerosol constituents with the in situ data, radiative closure was obtained through simulations performed with a polarimetric radiative transfer code, demonstrating the ability to constrain the black carbon mass fraction to approximately 5%, given the uncertainties in the AirMSPI measurements and the assumption of external mixing of aerosol components. The AirMSPI retrieval, made using a limited set of observations from the 470 nm polarimetric spectral band alone, was also generally consistent with operational retrievals of aerosol optical depth and surface reflectance made by the Multi-Angle Implementation of Atmospheric Correction algorithm at 1 km resolution.

Plain Language Summary The sensitivity of polarimetric remote sensing imagery to the black carbon content of wildfire smoke was demonstrated using the results of a NASA field campaign that took place over central California in July 2016. The chemical contents of the smoke plume were measured by an aircraft flying inside the smoke. This information was used to build a model of the smoke that was then used to estimate what would be observed by the remote sensing instrument. Good agreement was achieved in terms of the total amount of aerosol, the brightness of the underlying surface, and the fraction of black carbon in the plume.

1. Introduction

The extent of land burned by both wildfires and prescribed burning and the length of the fire season in the United States have increased dramatically in recent years, as shown in Figure 1. Based on data from the National Interagency Fire Center, the annual increase in the area burned in the United States is about 800 km^2/year. Dennison et al. (2014) reported similar trends for large wildfires in western states. Together, wildfires and prescribed burning, so-called "landscape fires," are estimated to produce about one third of the total airborne particulate matter (PM) in the United States (Park et al., 2007; Watson, 2002); and, in the western states,

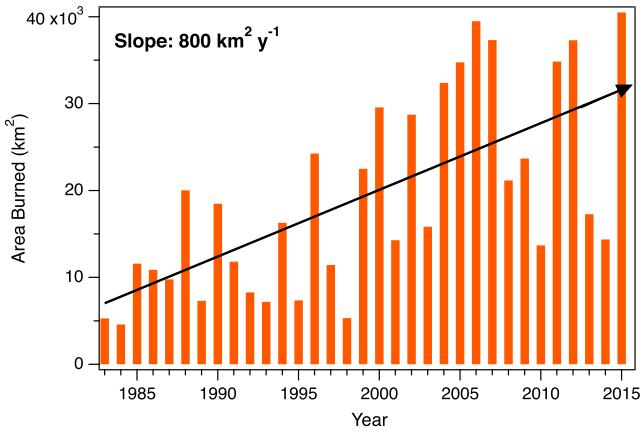

Figure 1. Area burned in the United States from 1983 to 2015 based on data from the National Interagency Fire Center. The trend line calculated using a nonparametric Theil-Sen estimator shows an annual increase in burned area of 800 km^2 per year following the approach of Dennison et al. (2014), who found similar trends for large wildfires in the western United States.

fires can contribute up to nearly 40% of the total PM emissions annually, and they dominate the overall PM emissions in months with greatest fire activity (Urbanski et al., 2011). Because population growth continues to enlarge the wildland-urban interface (Hammer et al., 2009), the potential for adverse health impacts associated with fire-emitted particulate components is increasing as well. In order for health professionals and decision makers to respond to the growing threat of fire emissions, increased understanding of landscape fire processes, smoke emissions, and downwind transport are essential.

While in situ and ground-based measurements can be used effectively at small scales to constrain smoke properties, larger-scale smoke plume characterization is more difficult. Although satellite remote sensing is useful for overall context, the temporal and spatial resolutions of satellite instruments are typically too coarse for detailed, process-oriented studies. Ideally, a quantitative chain of verification could be established linking detailed laboratory and airborne in situ measurements to satellite observations of smoke plumes from landscape fires. This, however, requires an intermediate stage of medium-scale, remote sensing observations made at resolutions on the order of tens of meters spatially and minutes temporally. State-of-the-art airborne

Table 1
NASA ER-2 and Navy CIRPAS Twin Otter Instruments and Products

Platform	Instrument	Science Product	Accuracy at High S/N ($\pm 1\sigma$)
NASA ER-2	Airborne Multiangle Spectro Polarimetric Imager (AirMSPI)	Spectropolarimetric intensities (10 m spatial resolution, eight wavelengths in 355–935 nm spectral range, three polarimetric bands)	3.0% absolute intensity, <0.5% degree of linear polarization
Navy CIRPAS Twin Otter	Aerodyne Aerosol Mass Spectrometer (AMS)	Submicrometer nonrefractory bulk aerosol chemical composition	17–19%
	Single Particle Soot Photometer (SP2)	Size-resolved aerosol BC mass	30%
	Scanning Mobility Particle Sizer (SMPS)	Aerosol particle size, 15 nm to 1μm	See Note
	Particle Soot Absorption Photometer (PSAP)	Absorption at 467, 530, and 660 nm	<20%
	Three-wavelength Integrating Nephelometer (TSINeph)	Wet and dry scattering at 450, 550, and 700 nm	2–10% for submicron mode

Note. The measurement accuracy values are taken from Diner et al. (2013) and Ryerson et al. (2013) for the AirMSPI and the CIRPAS instruments, respectively. Uncertainty of fine mode aerosol number is $\pm(9\% + 14/cm^3)$, surface area is $+(17\% + 0.2\ mm^2/cm^3)$, $-(8\% + 0.2\ mm^2/cm^3)$, and volume is $+(26\% + 0.03\ mm^3/cm^3)$, $-(12\% + 0.03\ mm^3/cm^3)$. NASA = National Aeronautics and Space Administration; CIRPAS = Center for Interdisciplinary Remotely-Piloted Aircraft Studies.

remote sensing instruments, such as imaging polarimeters, could potentially contribute to such efforts by generating high-resolution aerosol property information over smoke-affected areas.

In this paper, we first briefly describe the Imaging Polarimetric Assessment and Characterization of Tropospheric Particulate Matter (ImPACT-PM) field campaign and discuss the suite of instruments on the two participating aircraft—the Naval Postgraduate School Center for Interdisciplinary Remotely-Piloted Aircraft Studies (CIRPAS) Twin Otter, and the National Aeronautics and Space Administration (NASA) ER-2 high-altitude research aircraft. The central observations of interest from the perspective of studying landscape fires took place on 8 July 2016 in the vicinity of Lebec, CA, where a wildfire was simultaneously observed by the two coordinated aircraft. We describe the in situ observations of this event and discuss the leading uncertainties in optically modeling the aerosols within the smoke plume. The in situ PM size and composition are provided by an Aerodyne Aerosol Mass Spectrometer (AMS), a Scanning Mobility Particle Sizer (SMPS), a Single Particle Soot Photometer (SP2), a Particle Soot Absorption Photometer (PSAP), and a nephelometer (see Table 1). The Airborne Multiangle SpectroPolarimetric Imager (AirMSPI) instrument (Diner et al., 2013) on the NASA ER-2 aircraft provides the key remotely sensed data, which is first used to derive the height of the smoke plume using a geometric approach. Then, a radiometric closure study is performed to assess the ability of a polarimetric radiative transfer model of the plume, constrained by the in situ observations, to match a limited set of AirMSPI measurements. This leads to an evaluation of the sensitivity of remotely sensed, multiangular, polarimetric observations to the amount of black carbon in a wildfire smoke plume. Finally, we discuss the results of this exercise, describe the significance for remote sensing retrievals, and mention potential next steps.

2. The ImPACT-PM Field Campaign

The ImPACT-PM field campaign was carried out in California's San Joaquin Valley (SJV) from 5 to 8 July 2016. The joint Jet Propulsion Laboratory (JPL) and California Institute of Technology (Caltech) study, supported by NASA, was conducted to evaluate the ability of multiangle, spectropolarimetric remote sensing to retrieve information on the distributions of atmospheric particle types, with emphasis on carbon-containing compounds—black carbon (BC) and organic carbon (OC). The main goal of the campaign was to advance the science needed to support air quality management policy with state-of-the-art remote sensing observations, which is one of the primary objectives of the planned Multi-Angle Imager for Aerosol (MAIA) satellite investigation, currently in development under the third NASA Earth Venture Instrument (EVI-3) Program. The SJV was chosen because it has among the highest PM concentrations in the United States, including BC from vehicular and industrial combustion, organic (brown) carbon emitted by motor vehicles and biomass burning, and inorganic aerosols (sulfates, nitrates, and ammonium; Young et al., 2016). AirMSPI observations from on board the NASA ER-2 research aircraft were collected in coordination with the suite of science instruments on the lower flying Navy CIRPAS Twin Otter aircraft (see Table 1).

Although selected targets included ground-based measurement sites operated by the U.S. Environmental Protection Agency (EPA) and the California Air Resources Board (CARB) in Fresno, Modesto, Visalia, and Bakersfield, the prime target of opportunity for the ImPACT-PM field campaign was a local wildfire, the Fort Fire, that occurred on 8 July 2016 near the town of Lebec, CA (see Figure 2). This event provided a unique opportunity to evaluate the sensitivity of remotely sensed, multiangular, polarimetric observations to the amount of black carbon in a wildfire smoke plume by combining information from in situ measurements made by the CIRPAS Twin Otter with AirMSPI remote sensing data to establish radiative closure through radiative transfer simulations.

2.1. Remote Sensing Instrumentation

The AirMSPI instrument (Diner et al., 2013) has been flying aboard the NASA ER-2 since October 2010 and has participated in a number of field campaigns in the United States and internationally. AirMSPI is an eight-band (355, 380, 445, 470, 555, 660, 865, and 935 nm) pushbroom camera system, measuring polarization (Stokes Q and U) in the 470, 660, and 865 nm bands, mounted on a gimbal to acquire multiangular observations over a $\pm 67°$ along-track range. The imaged area typically covers about 10 km $\times$ 11 km with 10-m pixel resolution from the 20-km altitude of the ER-2 aircraft. AirMSPI has been demonstrated to have a high sensitivity to aerosol optical properties with $\sim$0.015 uncertainties in aerosol optical depth (AOD) and 0.03 in single-scattering albedo (SSA) as compared with ground-based validation data sets over both ocean (Xu et al., 2016) and land (Xu et al., 2017) targets. Intercomparison of AirMSPI aerosol property retrievals from observations collected during recent field campaigns with collocated ground-based measurements from the Aerosol Robotic Net-

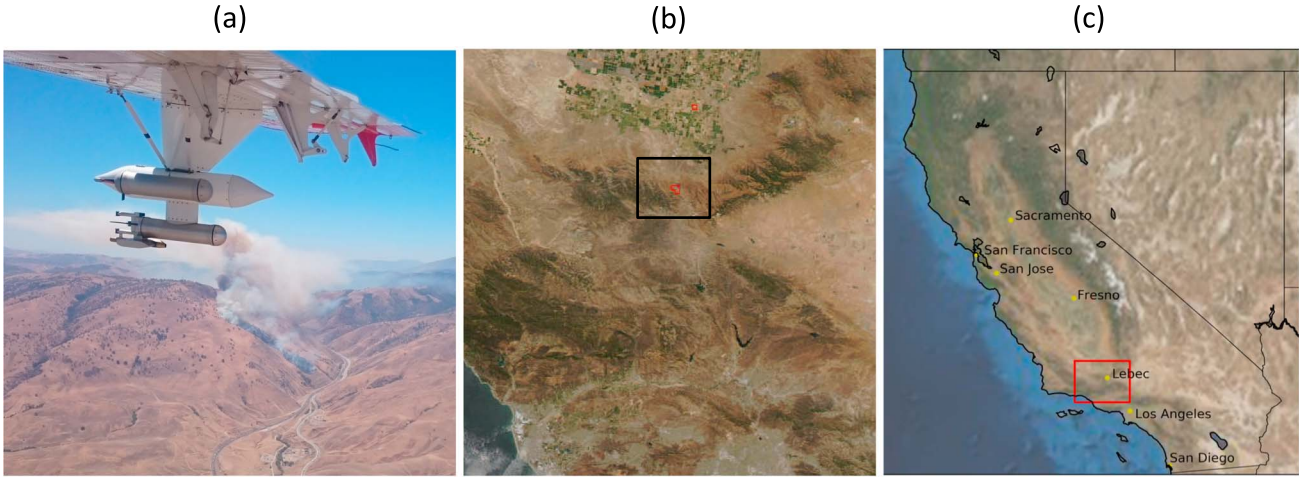

Figure 2. (a) Fort Fire near Lebec, CA photographed from the Center for Interdisciplinary Remotely-Piloted Aircraft Studies Twin Otter aircraft on 8 July 2016 at around 12:03 PDT (19:03 UTC); (b) MODerate resolution Imaging Spectroradiometer (MODIS) red-green-blue 250 m resolution image with MODIS thermal anomaly pixels (red boxes) indicating the fire near Lebec from MODIS-Aqua around 14:10 PDT (21:10 UTC granule; Image credit National Aeronautics and Space Administration/Goddard Space Flight Center, Rapid Response); (c) overview map showing the location of Lebec, CA (red rectangle).

work (AERONET; Holben et al., 1998) yielded AOD regressions with an R^2 of 0.95, a slope of 0.97, and an intercept of ~0.01, which reflect the high quality of aerosol retrievals based on AirMSPI data. While SSA and refractive index validations show relatively larger differences between AirMSPI and AERONET retrievals, the differences are generally within their respective uncertainties (Xu et al., 2017).

2.2. In Situ Instrumentation

In situ measurements of aerosol particle size, composition, and optical properties were made aboard the Navy CIRPAS Twin Otter aircraft, using an SMPS, AMS, SP2, PSAP, and nephelometer (Table 1). The SMPS, consisting of a differential mobility analyzer (DMA; TSI model 3081) coupled to a condensation particle counter (CPC; TSI model 3010), measured particle size distributions between ~15- and 1,000-nm diameter every 90 s. The SMPS was calibrated before the campaign using polystyrene latex spheres. The High-Resolution Time-of-Flight AMS (HR-ToF-AMS; Aerodyne Research, Inc.) quantified submicrometer, nonrefractory aerosol chemical composition and provided chemical speciation of sulfate, nitrate, ammonium, chloride, and organic components with a frequency of 0.1 Hz. The HR-ToF-AMS, described in more detail by DeCarlo et al. (2006), uses an aerodynamic lens to focus submicrometer aerosol onto a resistively heated surface (~600°C), where the particles undergo vaporization and electron impact ionization (70 eV), and the resulting ions are measured in a time-of-flight mass analyzer. On the aircraft, the sample flow rate into the AMS was maintained at ~1.4 cm^3/s using a pressure-controlled inlet. Spectra were analyzed using the SQUIRREL (v. 1.56D), and PIKA (v. 1.15D) modules for IGOR Pro (v. 6.36, WaveMetrics, Inc.), and were corrected for gas-phase interferences (Aiken et al., 2008; Allan et al., 2004) and composition-dependent collection efficiencies (Middlebrook et al., 2012). Detection limits for each chemical component were calculated as 3 times the standard deviations measured on filter samples before each flight, and the instrumental ionization efficiency was calibrated using atomized ammonium nitrate particles after each flight.

Particle total scattering was measured using a three-wavelength nephelometer (Radiance Research) with a correction for angular truncation applied; here only the measurements at 550 nm are used. Particle absorption was measured using a three-wavelength particle soot absorption photometer (PSAP; Radiance Research). The PSAP absorption data were corrected for filter loading and scattering artifacts as in Virkkula (2010). The single particle soot photometer (SP2; Droplet Measurement Technologies, Inc.) measured refractory BC mass concentrations and BC-specific size distributions (Schwarz et al., 2008). The SP2 was calibrated before each flight using dried, size-selected fullerene soot particles, and the size-dependent counting efficiency was determined by comparison with the particle concentration measured by a condensation particle counter. The BC detection efficiency fell off precipitously below 67 nm volume equivalent diameter, and thus, only data for particles larger than that size are included in the analysis. The mass contained in particles smaller than this threshold was estimated by fitting a log-normal distribution to the observed mass-weighted distribution. For the Fort Fire plume observations described below, the amount of undetected BC mass was

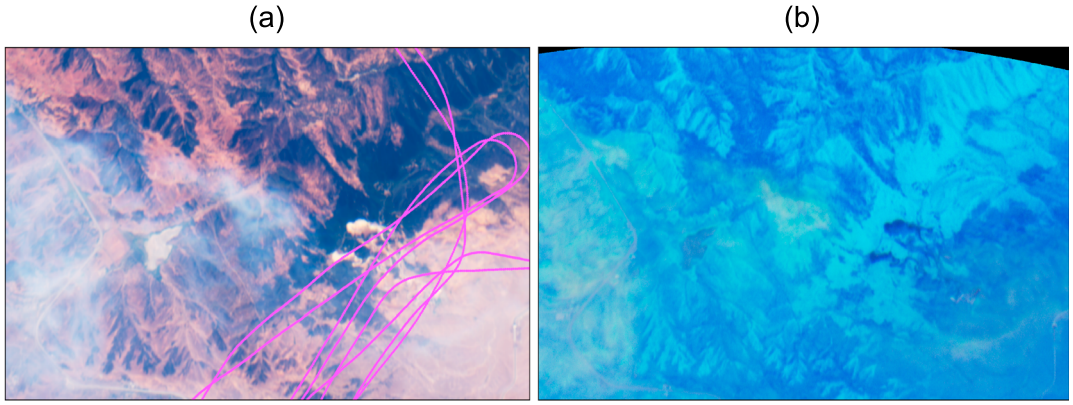

Figure 3. (a) Airborne Multiangle SpectroPolarimetric Imager (AirMSPI) true-color image of the Fort Fire from the 60° aftward view, covering an area of about 17.4 km east-west and 11.6 km north-south—a total of 202 km^2. The smoke appears as bluish-white, in contrast to the browns and greens of the surface. The Center for Interdisciplinary Remotely-Piloted Aircraft Studies Twin Otter flight tracks in the area are shown in magenta. (b) AirMSPI color composite image of the Fort Fire showing degree of linear polarization (DoLP), which depicts the smoke as greenish yellow over the bluish surface in these spectral bands.

estimated in this manner to be ~13%. Similarly, log-normal fits to the number-weighted BC size distributions were performed to estimate the number-weighted size distribution from 10 to 500 nm for use in Mie theory calculations.

2.3. Fort Fire Observations

A signature event of the ImPACT-PM campaign was the Fort Fire, a wildfire that began around 11:15 Pacific daylight time (PDT; 18:15 UTC, universal time coordinated) on 8 July 2016 in the vicinity of Lebec, CA, on the Tejon Ranch property near Interstate-5. The fire eventually burned 2.24 km^2 of primarily grass and scrub before it was extinguished the next day. The ER-2 and the Twin Otter coordinated to overfly the fire around 13:30 PDT (20:30 UTC). AirMSPI imaged smoke from the wildfire for about 7 min, centered at 13:19:46 PDT (20:19:46 UTC). Instruments on the Twin Otter sampled the smoke plume from 13:15 to 13:50 PDT (20:15 to 20:50 UTC), while the aircraft was circling in the downwind smoke layer to the east of the fire itself. Figure 2a shows a photograph of the smoke plume looking to the west taken at 12:03 PDT (19:03 UTC) from the Twin Otter more than an hour before the coordination with the ER-2. While flying in the smoke plume the Twin Otter altitude varied between 1,445 and 1,678 m above mean sea level (MSL), but the aircraft did not fly above the smoke layer. The Fort Fire was detected as a temperature anomaly by the MODerate resolution Imaging Spectroradiometer (MODIS) instrument on the NASA Aqua Earth Observing System (EOS) satellite that imaged the area around 14:10 PDT (21:10 UTC; Figure 2b).

Figure 3a shows the region imaged by the 60° aftward AirMSPI view in true-color intensity with the Twin Otter flight tracks overlaid in magenta. Figure 3b shows the same view in degree of linear polarization (DoLP). The color of the smoke in the polarization image shows that the particles in the smoke plume polarize the light differently than the light scattered from the underlying surface. Figure 4 shows aerosol mass concentrations retrieved from the AMS (green) and SP2 (black). The AMS measures mainly inorganic particles such as nitrate, sulfate, ammonium, and chloride, and organic compounds, while the SP2 measures BC concentrations. Figure 4 also shows the particle size distributions derived from the SMPS at two locations: Bakersfield (blue) acquired at 11:46 PDT (18:46 UTC), and Lebec (brown) acquired at 13:19 PDT (20:19 UTC). Particles measured downwind of the Fort Fire have larger concentrations and larger mean diameters than those measured in relatively polluted conditions near Bakersfield, where, in the summertime, secondary organic aerosols are dominant (Liu et al., 2012) and which also has much less BC.

The mass-weighted BC size distribution measured by the SP2 instrument within the Fort Fire plume can be approximated as log-normal with a median volume-equivalent diameter of 149 nm. Note that this is somewhat smaller than the size of the aerosol reported by the SMPS shown in the inset in Figure 4. This size is also somewhat smaller than that reported for most other biomass burning-impacted measurements, which typically have median volume-equivalent diameters closer to 200 nm (Kondo et al., 2011; Sahu et al., 2012; Schwarz et al., 2008; Taylor et al., 2014). The observed BC mass median diameter does, however, compare

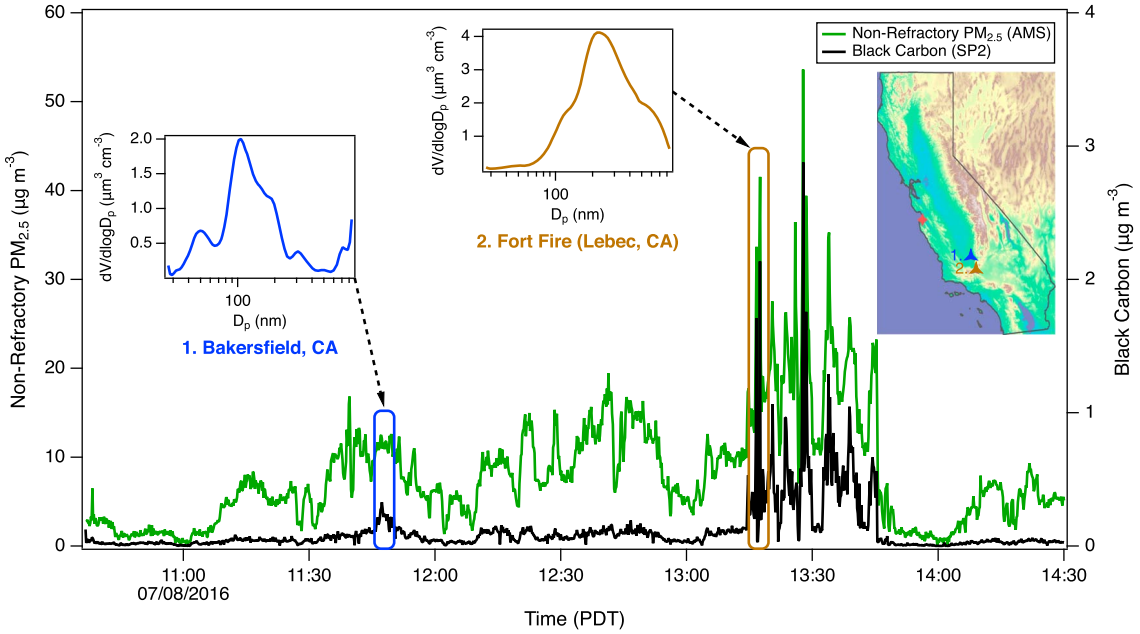

Figure 4. Total Aerosol Mass Spectrometer-measured aerosol mass concentration (green) and the SP2-derived black carbon mass concentration (black) during the 8 July 2016 flight over the San Joaquin Valley and Ventura County. Note the increased mass concentration during the 13:20–13:50 Pacific daylight time (PDT; 20:20–20:50 UTC, universal time coordinated) flight line over the smoke. Inset plots show the aerosol size distribution measured by Scanning Mobility Particle Sizer at the time of the Airborne Multiangle SpectroPolarimetric Imager (AirMSPI) overpass over Bakersfield, CA, at 11:47 PDT (18:47 UTC) and aerosol size distributions measured during the AirMSPI/Twin Otter coordination over the Fort Fire near Lebec, CA, at 13:30 PDT (20:30 UTC).

favorably to preliminary measurements for fresh BC from laboratory biomass combustion of a wide variety of different fuel types (average = 159 ± 20 nm; C. D. Cappa, initial FIREX data analysis).

In order to better characterize the vertical distribution of the smoke, we looked at hourly, ground-based observations of particulate matter with aerodynamic diameter less than 2.5 μm ($PM_{2.5}$) at the Lebec CARB site reported by the beta attenuation monitor (BAM). These data indicate that smoke from the Fort Fire extended to the ground during the time of the AirMSPI overpass. In the hourly BAM data, shown in Figure 5, the $PM_{2.5}$ concentration spiked to 45 μg/m^3 at local noon (19:00 UTC) from a background level as low as 4 μg/m^3 reported 1 hr earlier at 11:00 PDT (18:00 UTC). Near the time of the airborne observations, at 13:00 PDT (20:00 UTC), the BAM reported a value of 60 μg/m^3. After this peak, there was a gradual decrease in $PM_{2.5}$ over the next few hours to a background level of 5 μg/m^3 at 19:00 PDT (02:00 UTC the next day). By way of comparison, the total aerosol mass concentration measured in the plume from the combined AMS and SP2 observations varied between 40 and 60 μg/m^3, in good agreement with the maximum value reported by the BAM. The correspondence between the mass concentrations measured by the aircraft in the plume and the BAM on the ground indicates that the smoke was fairly well mixed down to ground level, consistent with the behavior of the plume shown in the photograph in Figure 2a.

Ground-based Sun-photometer measurements were not available in the vicinity of the Fort Fire to provide a reference for the total column aerosol optical loading described in terms of the AOD. The 3-km resolution Collection 6 (C6) MODIS Dark Target AOD product did not yield any useful data in this case, most likely due to the complex terrain (see Figure 6). However, remote sensing retrievals using MODIS data and the 1-km Multi-Angle Implementation of Atmospheric Correction (MAIAC) algorithm yielded an AOD of about 0.22 with a spatial standard deviation of ±0.03 at 470 nm in the vicinity of the downwind smoke sampled by the Twin Otter. The surface reflectance at this wavelength in the same area has a mean of 0.09, with a spatial standard deviation of ±0.02. MAIAC is an advanced aerosol retrieval algorithm that uses time series analysis and a combination of pixel- and image-based processing to improve accuracy of cloud detection, aerosol retrievals, and atmospheric correction, and it works well over desert and complex terrain yielding high-resolution retrievals of aerosol and surface properties (Lyapustin et al., 2011). In particular, MAIAC provides suites of gridded 1-km atmosphere and surface products, including the following: cloud masking, column water vapor, AOD, aerosol type (background, biomass burning, or dust), surface spectral bidirectional reflectance factors (BRFs), sur-

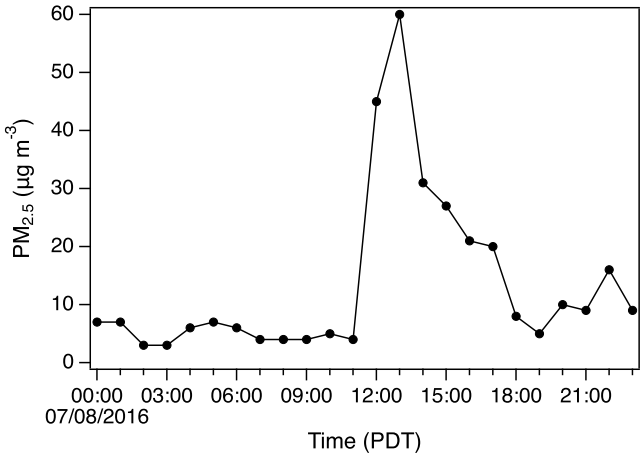

Figure 5. $PM_{2.5}$ measured through the day of 8 July 2016 by the California Air Resources Board beta attenuation monitor station near Lebec, CA (34.84155°N, −118.86058°E, 1,069 m elevation). The effects of the Fort Fire on the ambient air quality can be seen in the peak concentration observed at 13:00 Pacific daylight time (PDT; 20:00 UTC, universal time coordinated).

face reflectance, and Ross-Thick Li-Sparse (RTLS) bidirectional reflectance distribution function (BRDF) model parameters in seven MODIS land bands. Figure 6 shows the AirMSPI red-green-blue (RGB) image of the smoke from the Fort Fire along with the MAIAC AOD and surface reflectance at 470 nm, the wavelength used in our polarimetric sensitivity studies, described below, subsetted to the AirMSPI imaged area. The C6 MODIS 3-km Dark Target AOD retrievals are shown for reference. The MAIAC surface reflectance is derived from an 8-day time series and is, therefore, not expected to be affected by the smoke. The ∼50 min time difference between the AirMSPI observation of the smoke plume and the MODIS overpass means that it is unlikely that the smoke and the reported AODs would be exactly coincident, but the overall agreement between AirMSPI image of the smoke and the locations of high AOD reported by MAIAC appears to be very good. Near-coincident meteorological observations made just off the lower right corner of the map at the Sandberg weather station (KSDB, 34.7436°N, −118.7242°E, 1,375 m elevation) at 13:48 PTD (20:48 UTC) show a temperature of 29°C, a relative humidity (RH) of 24%, and winds out of the south at 6.2 m/s, gusting to 9.3 m/s, with consistent wind speeds and directions for the previous 3 hr. This suggests that the spatial pattern of the smoke would likely be more or less consistent during this time frame.

3. Methodology and Optical Modeling

Atmospheric aerosols, which are complex, heterogeneous mixtures of liquids and solids, can undergo aging processes that change their physicochemical and optical properties leading to complex internal mixtures of components. As a first step in characterizing the aerosol in the smoke plume downwind from the Fort Fire, we employ the AMS and SP2 measured aerosol species fractions to determine the relative contribution of different components to the overall spectropolarimetric signal that would be observed by AirMSPI. To simplify the polarimetric radiative transfer calculations, we assume that all particles are externally mixed; that is, each individual particle consists of only a single component, such as sulfate, organics, or BC. The idealized assumption of aerosol external mixing is expected to lead to biases in the calculated bulk aerosol optical properties, especially for BC-containing particles. For example, depending on the local RH and the amount of BC, the SSA values of an externally mixed aerosol could be 2% to 5% higher than those for an internally mixed aerosol with a BC core and a sulfate-nitrate-ammonium (SNA) or OC shell (Drury et al., 2010; Wang & Martin, 2007). These uncertainties are well within the expected error tolerance of our optical modeling and radiative transfer approaches, and the assumption of external mixing is commonly used in satellite remote sensing retrievals due to the computational expense of correctly evaluating coated, internally mixed particles.

The RH measured by the CIRPAS Twin Otter meteorological sensors in the smoke plume was, on average, 30%, and did not exceed 35%, in good agreement with the 24% RH reported at the nearby weather station. Particle water uptake tends to be small for RH < 35% (Hess et al., 1998); therefore, the optical properties of the aerosol components were assumed to correspond to dry particle conditions. To derive the in situ, chemically speciated, submicrometer particulate mass concentrations in the plume shown in Figure 7a, the AMS

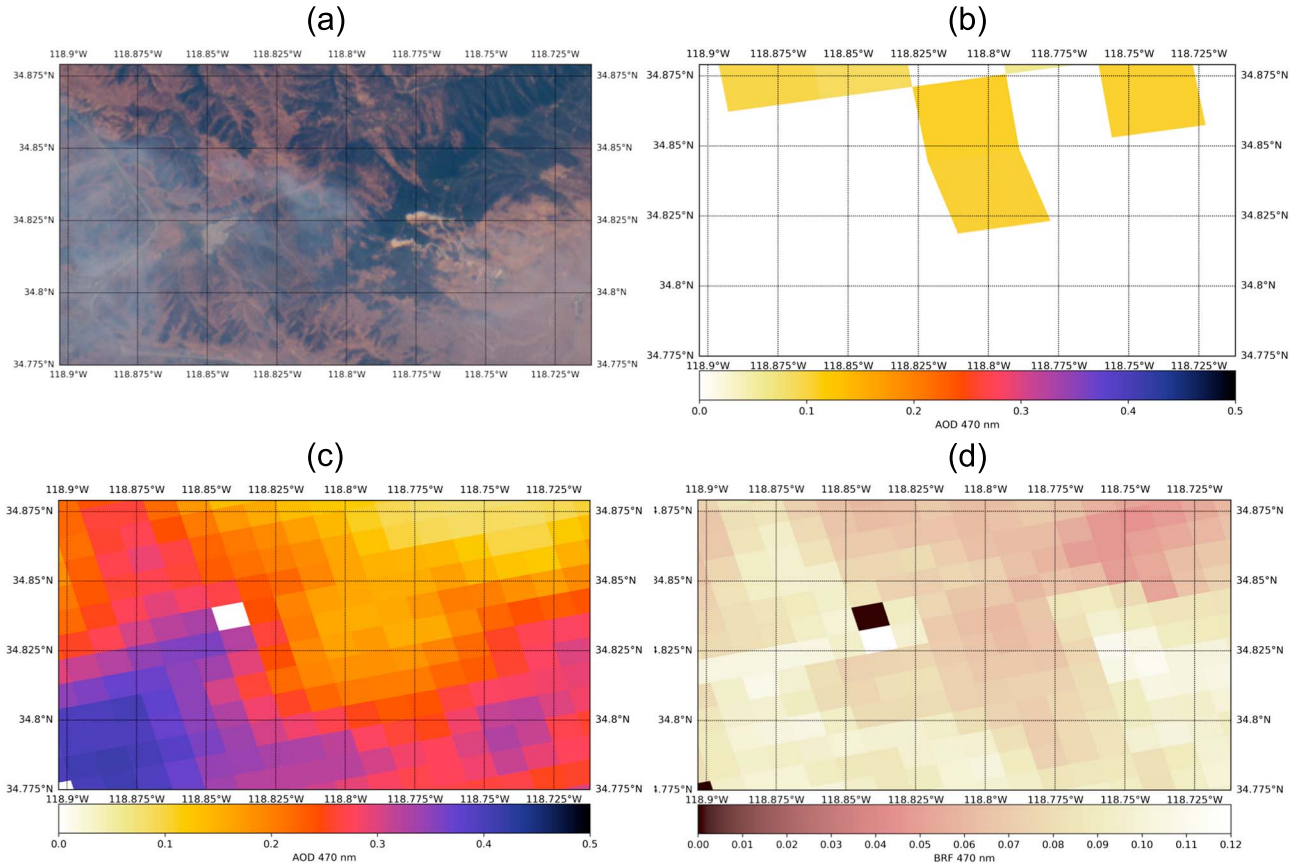

Figure 6. (a) Airborne Multiangle SpectroPolarimetric Imager (AirMSPI) red-green-blue image of the Fort Fire smoke plume area at 13:22 PDT (20:22 UTC) on 8 July 2016; (b) MODerate resolution Imaging Spectroradiometer (MODIS) C6 Dark Target 3-km aerosol optical depth (AOD) at 470 nm from 14:10 PDT (21:10 UTC) matched to AirMSPI-imaged area; (c) Multi-Angle Implementation of Atmospheric Correction (MAIAC) MODIS Aqua 1-km resolution aerosol optical depth at 470 nm; (d) Lower right panel: MAIAC 1-km surface reflectance at 470 nm. BRF = bidirectional reflectance factor.

and SP2 data were averaged over the period during which the SP2 indicated the presence of large amounts of BC—13:15:33 to 13:46:11 PDT (20:15:33 to 20:46:11 UTC)—excluding samples taken while the plane was turning around outside the plume. During this time, the particles were primarily composed of organics (73.1% ± 0.9%), followed by sulfate and nitrate in approximately equal abundance (9.0% ± 1.3% and 7.4% ± 0.4%, respectively), then BC (5.0% ± 0.9%), ammonium (3.5% ± 0.5%), and chloride (2.0% ± 0.6%). The ranges correspond to 1 standard deviation of the values measured within the plume. The ion balance suggests that the particles were somewhat acidic.

The SP2-derived average BC mass within the plume seems relatively small for wildfire smoke, only 5%. Laboratory observations of fire-derived particles show that the BC fraction can vary over a wide range, depending on the fuel type and burning conditions, which are interrelated (McMeeking et al., 2009, 2014). A 5% BC mass fraction is consistent with visual observations of the smoke plume during the encounter. As seen in Figure 2a, the smoke appears primarily white or light brown instead of black, suggesting little light absorption and, therefore, a small BC content. The fuel type for the Fort Fire was predominantly dry grass and scrub, which might also imply less BC emission in a smoldering phase (Chow et al., 2010). However, OC/BC fractions show a high degree of variability, both between and within different fuel types and species (Jolleys et al., 2014), making the amount of BC difficult to evaluate based on the fuel type alone. Other field observations within major wildfire plumes in California yielded similarly small BC mass fractions (sometimes as low as 2–3%), although again dependent on burning conditions (Kondo et al., 2011).

In order to use the aerosol components determined from the in situ AMS and SP2 observations in radiative transfer calculations, measured mass fractions were converted to volume fractions based on their assumed bulk densities. While the inorganic species (sulfate, nitrate, ammonium, and chloride) should technically be apportioned to their constituent salts and scaled by those densities (ammonium sulfate = 1.78 g/cm^3,

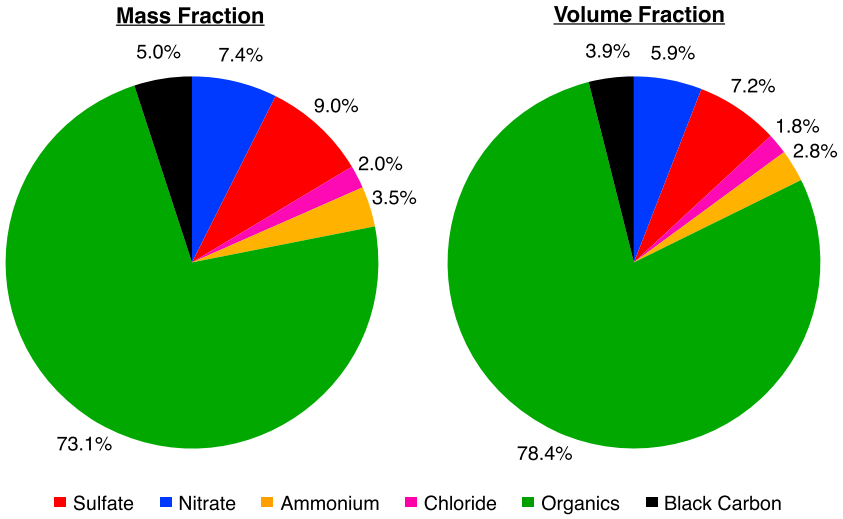

Figure 7. (left) In situ chemically speciated submicrometer particulate mass fractions in the smoke plume from the Center for Interdisciplinary Remotely-Piloted Aircraft Studies Twin Otter, obtained assuming that the total aerosol mass concentration is given by the sum of SP2 measured mass concentration of BC and AMS-derived mass concentrations of sulfate, nitrate, ammonium, chloride, and organics; (right) Volume fractions of submicrometer aerosol components derived from AMS and SP2 measured mass and assumed bulk densities.

ammonium nitrate = 1.72 g/cm^3, ammonium chloride = 1.52 g/cm^3), the SNA component was assigned a density of 1.75 g cm^{-3}, and chloride was assigned a density of 1.52 g cm^{-3} (Salcedo et al., 2006). The density of the organic component depends on the specific composition and usually lies between 1.0 and 1.4 g/cm^3. AMS O/C and H/C ratios were used to estimate the density of the organic components following the approach of Kuwata et al. (2012). Based on those data points within the plume used to derive the mass fractions shown in Figure 7a, the O/C ratio was determined to be 0.555 and the H/C ratio was found to be 1.6, yielding a density of 1.3 g/cm^3 for the organics, the value adopted here. There is continuing discussion in the literature concerning the density of BC particles (Bond et al., 2013). Following Park et al. (2004), a value of 1.8 g/cm^3 was adopted. Derived particle volume fractions are shown in Figure 7b.

Refractive indices for the different aerosol components are also needed for radiative transfer calculations. The refractive indices for sulfate and OC were taken from the Optical Properties of Aerosols and Clouds (OPAC) database used in the Global Aerosol Data Set (GADS) (Hess et al., 1998; Koepke et al., 1997), and currently used in the Goddard Earth Observing System (GEOS)-Chem model (Martin et al., 2003). Following the GEOS-Chem implementation (Martin et al., 2003), the refractive indices of nitrate, ammonium, and chloride were taken to be identical to those of sulfate. Refractive indices of BC, which continue to be a subject of attention in the literature (Stier et al., 2007), were varied in the range suggested by Hess et al. (1998) and Bond and Bergstrom (2006), as described in greater detail below.

The number-weighted log-normal size distribution parameters measured by the in situ instruments at the time of the AirMSPI overpass were used with the appropriate refractive indices in Mie calculations assuming spherical particles (Mishchenko et al., 1999). While flaming fires are known to produce long-chain aggregates of particles, the assumption of particle sphericity for smoldering-dominated fires and transported smoke is typically adequate (Reid et al., 2005). For example, Chakrabarty et al. (2014) examined a large number of scanning electron microscope (SEM) filters taken from a range of different wildfires and found that large particle aggregates were only common for samples taken near the source of flaming fires and nearly completely absent in samples taken from organic carbon-dominated smoldering fires.

Particle size distributions for the different individual components were based on SMPS and SP2 measurements through log-normal fits to the data:

$$n(r) = \frac{N}{(2\pi)^{\frac{1}{2}} r \cdot \ln\sigma} \cdot \exp\left[\frac{-(\ln r - \ln r_c)^2}{2(\ln\sigma)^2}\right], \quad (1)$$

where n is the number of particles, N is a scaling factor, r is the particle radius, r_c is the characteristic (median) radius, and σ is the width of the distribution. The number-weighted, log-normal fit to the SP2 measurements

Table 2
Aerosol Size Distribution Parameters for Number-Weighted, Log-Normal Size Distributions Derived from SP2 and SMPS Observations in the Smoke

	OC	BC	SNA
Median diameter (μm)	0.10–0.15 (0.11)	0.05–0.08 (0.08)	0.10–0.15 (0.11)
Width of the size distribution (σ)	1.45–1.65 (1.6)	1.1–2.1 (1.6)	1.45–1.65 (1.6)

Note. Values in parentheses correspond to those used in the Mie calculations. SP2 = Single Particle Soot Photometer; SMPS = Scanning Mobility Particle Sizer; OC = organic carbon; BC = black carbon; SNA = sulfate-nitrate-ammonium.

in the smoke plume implies a BC median diameter in the range from 50 to 80 nm, and width of the log-normal distribution of 1.1 to 2.1. The size distribution parameters are listed in Table 2 and the parameters adopted for the Mie calculations are shown in parentheses. Particle refractive indices interpolated to AirMSPI midvisible and NIR wavelengths are summarized in Table 3, which contains the values from Hess et al. (1998) as well as from Bond and Bergstrom (2006), the latter of which assumes the same spectral dependence as those from Hess et al. (1998).

We recognize that OC absorption at short visible wavelengths is affected by the presence of brown carbon (BrC) released by the combustion of organic matter, resulting in a larger value of the imaginary part of the refractive index at short visible wavelengths. This may limit the applicability of the Hess et al. (1998) refractive indices for the OC component in fire emissions. However, measurements show that the imaginary part of the refractive index in smoke is relatively constant for wavelengths longer than 440 nm (Mok et al., 2016), which yields relatively small deviations from the BC-predicted spectral slope of SSA at midvisible and near-infrared wavelengths (Liu et al., 2014). Since the radiative transfer calculations are performed for the shortest polarized wavelength of AirMSPI, 470 nm, we argue that the presence of BrC in the smoke plume will likely only have a minimal impact on our results.

Knowing the aerosol refractive indices and the size distribution for each species, j, the aerosol phase matrix, $P_j(\Theta)$, extinction coefficient, $K_{\mathrm{ext},j}$, scattering coefficient, $K_{\mathrm{sca},j}$, and SSA, ϖ_j were computed using Mie theory (Mishchenko et al., 1999). Field measurements show that smoke aerosols are typically spherical, to a good approximation, at some distance from the source, as is the case for the AirMSPI and CIRPAS Twin Otter observations of the Fort Fire plume (Martins et al., 1998; Reid et al., 2005). Figure 8 shows elements of the scattering phase matrix for SNA, OC, and BC calculated using the OPAC refractive indices for the three polarized AirMSPI wavelengths—470 nm (blue), 660 nm (red), and 865 nm (magenta). The P11 element of the phase matrix describes the effect of single scattering on intensity, while the P12 element describes the linear polarizing effect of single scattering on unpolarized incident radiation. The ratio of the these two represents the DoLP induced by single scattering. In all cases, for these relatively small particles, the maximum DoLP is almost 100% near a scattering angle of 90°, similar to Rayleigh scattering. The vertical lines indicate the AirMSPI viewing geometry for the Fort Fire case. As this example shows, the AirMSPI observations cover a wide range of scattering angles from 110° to 170°. Importantly, AirMSPI observes the backscattering portion of the phase matrix where significant differences exist among the scattering by different aerosol types. This illustrates how AirMSPI spectropolarimetric observations can be used to characterize atmospheric aerosols.

Table 3
Refractive Indices for Organic Carbon (OC), Black Carbon (BC), and Sulfate-Nitrate-Ammonia (SNA) Interpolated to AirMSPI Wavelengths

	OC		BC				SNA	
λ (nm)	n_r	n_i	n_r (Hess)	n_i (Hess)	n_r (Bond)	n_i (Bond)	n_r	n_i
470	1.530	5×10^{-3}	1.750	0.4530	1.850	0.7230	1.432	1×10^{-9}
555	1.530	5×10^{-3}	1.750	0.4395	1.850	0.7095	1.430	1×10^{-9}
660	1.530	5×10^{-3}	1.750	0.4340	1.850	0.7040	1.429	1×10^{-9}
865	1.520	5×10^{-3}	1.750	0.4333	1.850	0.7031	1.425	1×10^{-9}
935	1.520	5×10^{-3}	1.753	0.4367	1.853	0.7067	1.422	1×10^{-9}

Note. Values for OC and SNA from Hess et al. (1998). BC values from Hess et al. (1998) and Bond and Bergstrom (2006).

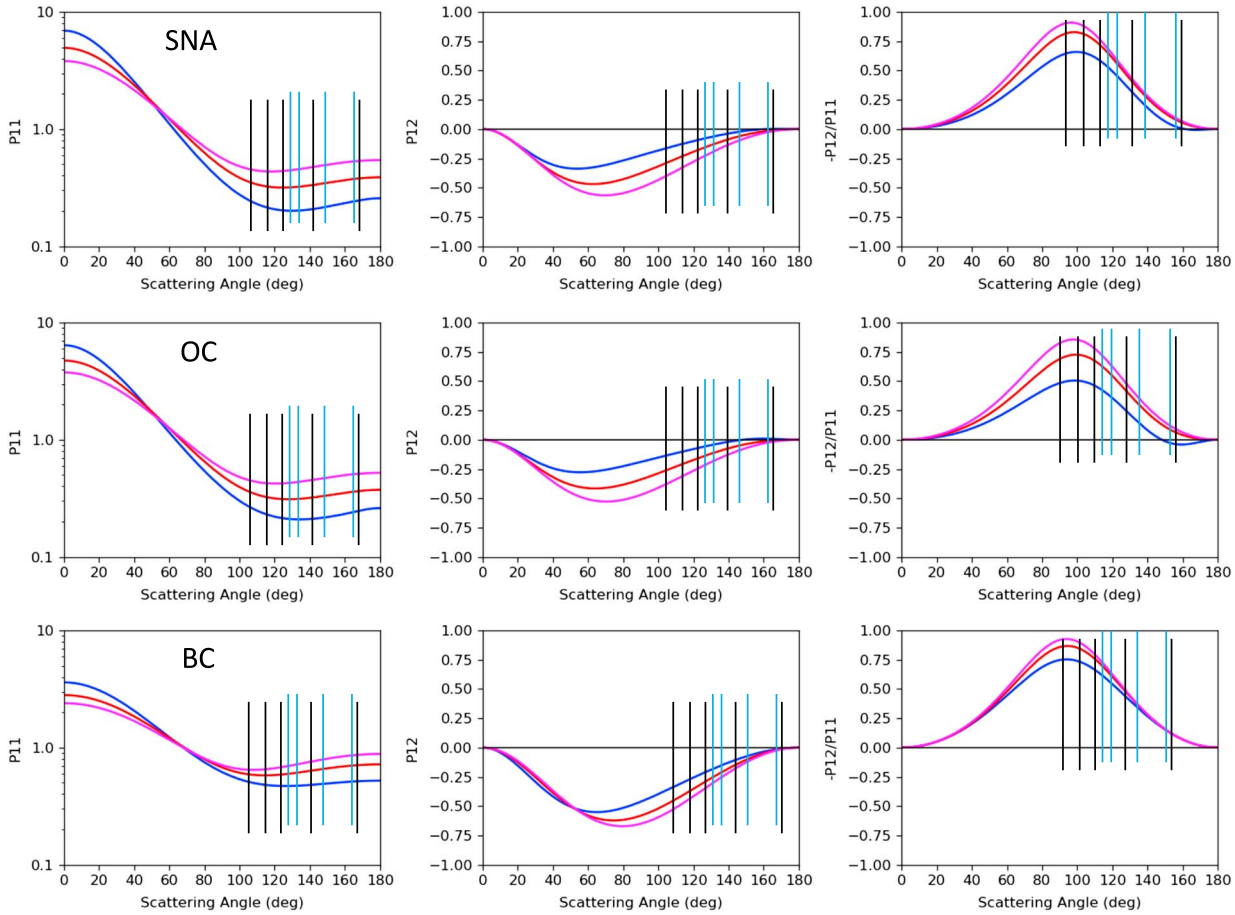

Figure 8. Phase matrix elements from Mie modeling at 470 nm (blue), 660 nm (red), and 865 nm (magenta) for Sulfate-Nitrate Ammonium (SNA) (top row); Organic Carbon (OC) (middle row); and Black Carbon (BC) (bottom row). Columns correspond to the elements P11 (left), P12 (middle), and the ratio of P12 to P11 (right). The Airborne Multiangle SpectroPolarimetric Imager viewing geometry for the Fort Fire case is overplotted with vertical black lines corresponding to forward viewing angles and vertical light blue lines corresponding to aftward viewing angles.

Using the single-scattering results for SNA, OC, and BC, the optical properties for the aerosol mixtures, which were assumed to be dry and externally mixed, were calculated as follows (Hess et al., 1998):

$$K_{ext}(\lambda) = \sum_j K_{ext,j}(\lambda) \tag{2}$$

$$K_{scat}(\lambda) = \sum_j K_{scat,j}(\lambda) \tag{3}$$

$$\varpi(\lambda) = \frac{K_{scat}(\lambda)}{K_{ext}(\lambda)} \tag{4}$$

$$P(\Theta, \lambda) = \frac{\sum_j K_{scat,j}(\lambda) \times P_j(\Theta, \lambda)}{K_{scat}(\lambda)} \tag{5}$$

for j corresponding to SNA, OC, and BC.

Figure 9a shows the spectral SSA of the resulting mixtures calculated using this approach for different BC mass concentrations, with the mass concentrations of the other components fixed to those reported by the AMS (i.e., ammonium = 0.77 μg/m^3; sulfate = 1.98 μg/m^3, nitrate = 1.61 μg/m^3, chloride = 0.43 μg/m^3, OC = 16.02 μg/m^3). The 1.1 μg/m^3 corresponds to 5% of the total mass fraction, which the SP2 assigns to BC. BC mass fractions were varied in the range from 5% to 20% to cover the range of smoke SSAs found in a variety of AERONET observations (Sayer et al., 2014). The resulting SSA spectral slopes demonstrate the expected

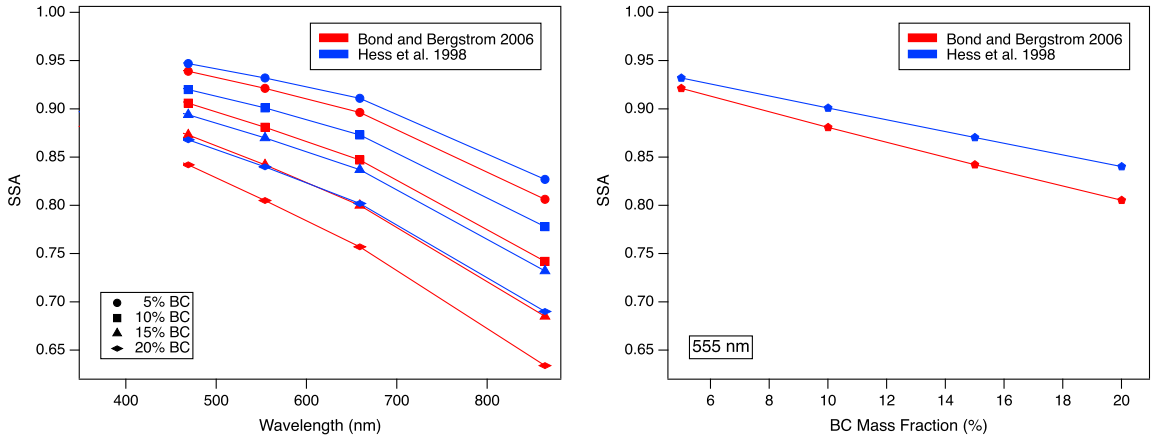

Figure 9. SSA calculated using Mie theory with prescribed optical properties for smoke aerosol based on Aerosol Mass Spectrometer-derived mass fractions assuming external mixing of components. (left) Single-scattering albedo (SSA) spectral dependence assuming black carbon (BC) mass concentrations from 5% to 20%; (right) SSA at 555 nm assuming BC mass concentrations from 5% to 20% and refractive indices for BC from Hess et al. (1998) and Bond and Bergstrom (2006).

behavior of BC-containing aerosols with near-spectrally invariant refractive indices, showing increasing absorption at longer wavelengths. Figure 9b compares the SSA at 555 nm as a function of BC mass fraction calculated with the different refractive indices for BC suggested by Hess et al. (1998) and Bond and Bergstrom (2006). The calculations are performed for the 555 nm AirMSPI wavelength in order to facilitate comparisons with the SSA values derived from the SP2 and the PSAP absorption measurements matched to the nephelometer scattering observations in the Fort Fire plume to evaluate the validity of the external mixing assumption and the representativeness of the selected range of BC mass concentrations.

Figure 10 shows the in-plume SSA at 550 nm derived from 10-s averaged (lightly shaded) and 1-min averaged (dark shaded) absorption data from the SP2 in gray and from the ratio of the PSAP absorption to the nephelometer scattering data in green. Short periods when the nephelometer scattering was less than 10 M/m were not included in the analysis to account for times when the Twin Otter was flying outside the plume. The absorption coefficient, b_{abs} (with units of M/m), from the SP2 was estimated from the directly measured BC mass concentration while the Twin Otter was within the plume as $b_{abs} = 7.5 \times [BC]$, where 7.5 is the mass absorption coefficient (MAC, m^2/g) for "pure" BC at 550 nm (Bond & Bergstrom, 2006). Typically, this MAC value is considered a lower bound for atmospheric BC since the presence of nonabsorbing coatings on BC can enhance the absorption and thus increase the apparent MAC (Fuller et al., 1999).

The plume-averaged b_{abs} from the SP2 was 3.3 ($\pm$2.7) M/m, while that estimated from the PSAP and nephelometer was 8.3 ($\pm$6.1) M/m. These values correspond to a plume-averaged SSA of 0.94 $\pm$ 0.01 (1σ) from the SP2 and 0.88 $\pm$ 0.04 (1σ) from the PSAP and nephelometer. However, the relatively large uncertainties reported here, which correspond to 1 standard deviation of the values determined while the Twin Otter was in the plume, show that there was substantial spatial variability in the absorption. The larger absorption and lower SSA derived from the PSAP and nephelometer data could also be a result of a bias due to the relatively large observed concentration of organic aerosol (OA) in the smoke plume, as organics are not fully accounted for in the filter loading correction. Biases as large as two or three have been observed previously when the OA/BC ratio was large (Cappa et al., 2008; Lack et al., 2008). Alternatively, the bias could be attributed to uncertainty in the MAC for BC (estimated at $\pm$1.2 m^2/g, not accounting for any potential enhancements) or in the SP2 BC mass concentration measurement itself. Finally, some of the difference between the SP2 and PSAP/nephelometer results might be due to absorption by non-BC species, specifically BrC. The PSAP absorption measurement includes contributions from non-BC species, while the SP2 estimate does not. For biomass combustion-derived particles, the contribution of BrC to total absorption depends on the fuel type, burning conditions, and wavelength, with larger BrC contributions at shorter wavelengths, but almost negligible differences at midvisible wavelengths (Kirchstetter et al., 2004; McMeeking et al., 2014; Pokhrel et al., 2017; Saleh et al., 2014; Zhang et al., 2016). Given that the SP2-derived SSA does not include potential contributions of BrC to the total absorption, it is possible that the SP2 estimate of absorption might be biased low; however, it is not likely to result in a difference of a factor of 2.5 in the absorption coefficient; 3.3 M/m for the SP2 compared to 8.3 M/m for the PSAP and nephelometer. This difference justifies testing BC concentrations ranging

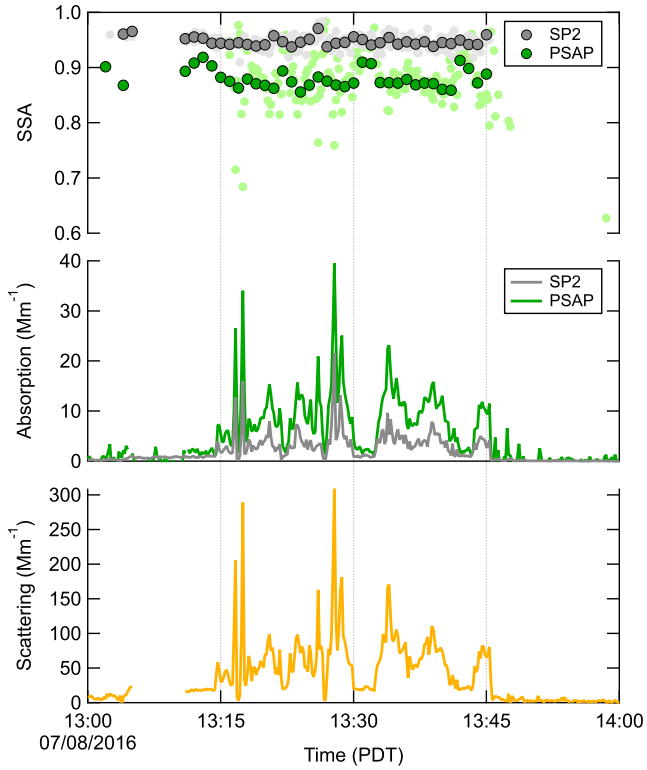

Figure 10. (top) Single-scattering albedo (SSA) at 550 nm in the Fort Fire smoke plume derived from Single Particle Soot Photometer (SP2) and Particle Soot Absorption Photometer (PSAP)/nephelometer observations. Light shading indicates 10-s averages in the plume, while dark shading corresponds to 1-min averages. The average SSA in the plume from the SP2 is 0.94 ± 0.01 (1σ), compared to 0.88 ± 0.04 (1σ) derived from the PSAP/nephelometer. (middle) Estimated absorption coefficient at 550 nm from the SP2 (gray) and the PSAP (green). (bottom) Extinction coefficient at 550 nm derived from the nephelometer.

from 5% to 20%, which changes the SSA of the aerosol mixtures by 0.06. Laboratory measurements of SSA values for smoke produced from biomass combustion demonstrate that the SSA for fresh, fire-derived particles can be highly variable, depending importantly on the fuel type (Chakrabarty et al., 2010; Griffin & Critchfield, 1972) and combustion conditions (Liu et al., 2014).

4. AirMSPI Observations and Closure Study

Closure studies, which are made possible by simultaneous remote sensing and in situ sampling, are helpful for evaluating spectropolarimetric sensitivities to BC fraction and deriving error estimates (Dubovik et al., 2011; Xu et al., 2016). In the case of the Fort Fire, we use radiative closure to attempt to resolve the differences in the BC content and SSA reported by the SP2 and the PSAP/nephelometer data. Recall that the average SSA at 550 nm in the smoke plume derived from the SP2 measurements was 0.94 ± 0.01 (1σ), compared to 0.88 ± 0.04 (1σ) derived from the PSAP/nephelometer measurements. Scattering models were constructed for smoke aerosols with differing fractions of BC ranging from 5% to 20%, corresponding to the observed range of SSAs, based on the in situ measurements of the composition from the AMS and SP2 (Figure 7) and the size distribution from the SMPS (Figure 4, inset). After addressing the issue of the apparent plume motion through the sequence of AirMSPI observations that can be used to derive the height of the plume, the remaining unknowns are the total column AOD for the smoke and the surface reflectance, which we take to be Lambertian, for simplicity. Closure, then, involves finding the AOD-surface albedo-SSA combination that yields the best agreement with the AirMSPI observations using full vector (polarimetric) radiative transfer modeling.

The height of the smoke plume causes its apparent location to shift from one view to the next through the sequence of AirMSPI observations due to parallax. This shift can be used to estimate the plume height geometrically following the method employed by the Multi-angle Imaging SpectroRadiometer (MISR) INteractive eXplorer (MINX) tool (Nelson et al., 2013). Well-defined features at the top of the plume observed at 470 nm

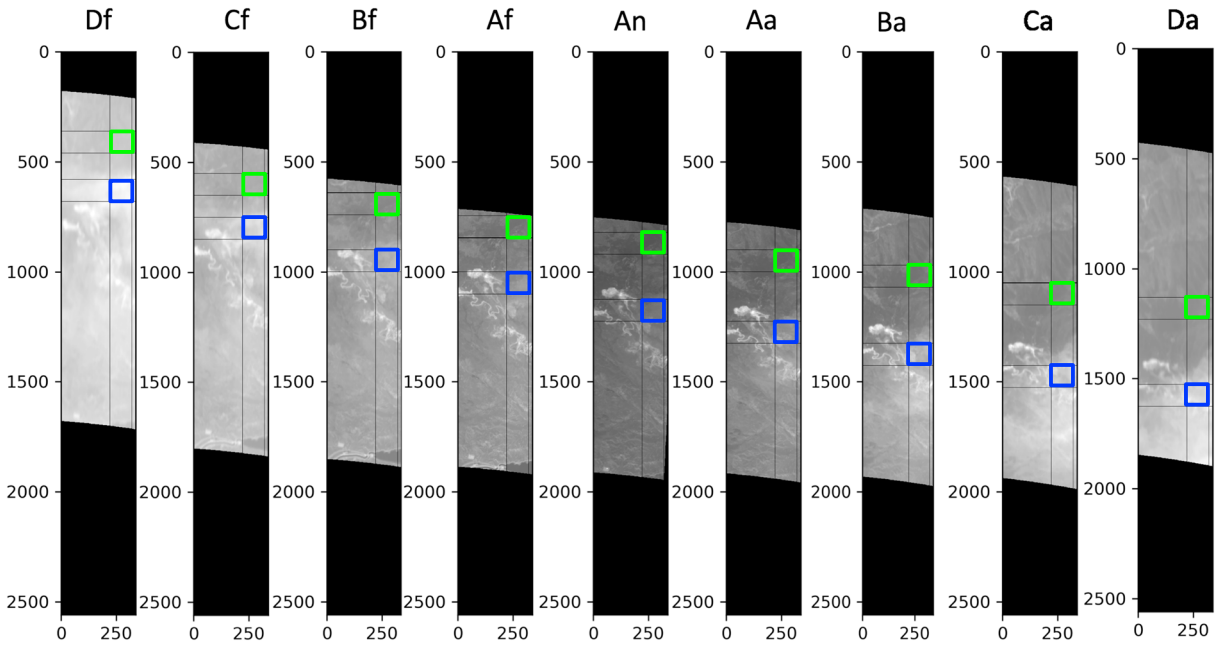

Figure 11. Airborne Multiangle SpectroPolarimetric Imager (AirMSPI) views of the Fort Fire smoke plume at 470 nm. Thin strips corresponding to the full length of the AirMSPI images with a width of approximately 3 km were selected to highlight the plume in the region where the Center for Interdisciplinary Remotely-Piloted Aircraft Studies Twin Otter was operating. The blue box shows the location of a 1 km^2 patch in the smoke plume tracked through the nine images. The Multi-angle Imaging SpectroRadiometer convention for the views is adopted here for convenience with Df = 68.4°, Cf = 61.2°, Bf = 50.2°, Af = 32.1°, An = 9.0°, Aa = 28.3°, Ba = 47.3°, Ca = 60.0°, and Da = 65.6°.

are tracked manually through multiple AirMSPI views as shown in Figure 11. A single band is selected because the spectral bands are offset in the direction of the flight motion (along-track) in the AirMSPI detector (Diner et al., 2013). Since AirMSPI is a pushbroom sensor, this offset leads to a shift in the location of features from band to band that is typically handled by the L1B2 processing, which coregisters the individual bands to "pixels" on the surface. The 470 nm band was selected because this is the shortest polarimetric wavelength in AirMSPI, smoke features are easier to identify due to the somewhat larger AOD, and the surface reflectance is expected to be fairly low. For example, the Advanced Spaceborne Thermal Emission Reflection Radiometer (ASTER) instrument on the Terra satellite has a spectral library (v2.0) that gives a reflectance of grass at 470 nm of 4.2% and of brown, gravelly, sandy loam of about 10% (Baldridge et al., 2009).

Two 1-km × 1-km boxes were manually "tracked" through the AirMSPI image sequence shown in Figure 11. The blue box corresponds to a feature at the top of the smoke plume. The green box is a "patch" of the same size corresponding to the surface in the clear air outside the plume. For convenience, the convention used by MISR is adopted here, with the triplet of angles closest to (and including) nadir being designated "A," the next most oblique pair of views designated "B," and so on (Diner et al., 1998). The spatial separation between the patches changes from view to view due to the height-induced parallax of the features associated with the smoke plume. The length of the strips in the image represents the full image swath of the AirMSPI L1B2 data in the along-track direction (in this case from south to north), which is common to all nine views. Taking only the shift in the along-track direction relative to the An (near-nadir) view a mean height of $2,700 \pm 200$ m is obtained for the smoke plume. The uncertainty reflects the standard deviation of the estimates of the stereo pairs (each individual view forms a pair with the An view). The height estimate also does not take into account motion of the plume due to the wind or higher-order details of the viewing geometry (Nelson et al., 2013). By way of comparison, the CIRPAS Twin Otter never flew high enough to be above the smoke. The maximum reported flight altitude of 1,800 m above mean sea level (ASL) is consistent with being inside a smoke plume with a top height of 2,700 m. For the subsequent radiative transfer calculations and AirMSPI data comparisons, we use the mean geometry from the selected 1-km × 1-km smoke patch (see Table 4).

Figure 12 shows the AirMSPI observations for the "Smoke" and "Clear" patches in the previous figure. Instead of working with the "raw" AirMSPI radiances, we convert them to bidirectional reflectance factors (BRFs) or

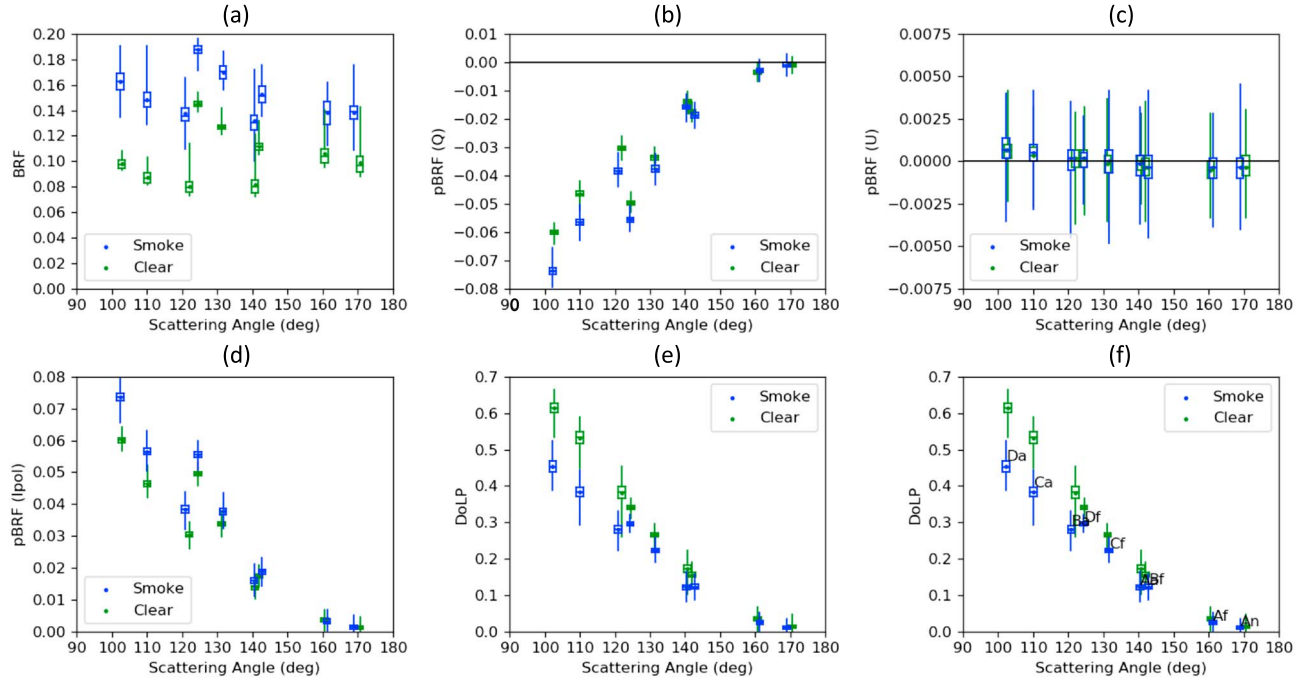

Figure 12. Airborne Multiangle SpectroPolarimetric Imager (AirMSPI) observations of the smoke and clear patches as a function of scattering angle. The box plots represent the variability of the AirMSPI 10 m^2 observations within the 1-km × 1-km patches. (a) BRF; (b) pBRF for Stokes *Q*; (c) pBRF for Stokes *U*; (d) Ipol; (e) DoLP; (f) DoLP with AirMSPI cameras labeled following the Multi-angle Imaging SpectroRadiometer convention.

polarized bidirectional reflectance factors (pBRFs), as appropriate. The BRF is given by the following relation:

$$\mathrm{BRF} = \frac{\pi I}{\mu_0 E_0}, \tag{6}$$

where I is the radiance observed by the instrument, μ_0 is the cosine of the solar zenith angle, and E_0 is the extraterrestrial solar spectral irradiance for the AirMSPI band (in this case 470 nm). By analogy, the pBRF for the *Q* component of the Stokes vector (representing the excess of horizontally over vertically polarized light), is given by

$$\mathrm{pBRF} = \frac{\pi Q}{\mu_0 E_0}. \tag{7}$$

Figure 12a shows box plots of the BRF observed by AirMSPI at 470 nm in the smoke plume and the nearby clear patch. The mean value is represented by a dot, the median value by a horizontal line, the interquartile range (25% to 75%) by the box, and the extremes by the whiskers. The results are presented as a function of the scattering angle, Θ, which is given by the equation

$$\cos\Theta = -\mu\mu_0 + \nu\nu_0 \cos\Delta\phi, \tag{8}$$

where μ is the cosine of the view angle, ν is the sine of the view angle, ν_0 is the sine of the solar zenith angle, and $\Delta\phi$ is the relative azimuth angle. Note that AirMSPI does not sample the scattering angles sequentially by view (see Figure 12f). Not surprisingly, the BRF of the smoke plume is larger than the BRF in the clear patch because, as shown in Figure 11, the smoke appears brighter in the AirMSPI images in all views.

Figure 12b shows box plots of pBRF for Stokes *Q*. In an absolute sense, the smoke appears more polarized than the clear region, especially at scattering angles near 100°. The total Rayleigh optical depth at 470 nm for an altitude of 1,000 m, which is the mean elevation of the area around Lebec, CA, is 0.1637 (Bodhaine et al., 1999). Therefore, both the clear and smoke patches have a significant Rayleigh contribution to the polarization, which reaches a maximum at a scattering angle of 90°. In the scattering plane observations reported by AirMSPI, the pBRF for the Stokes *U* component (excess of 45° over 135° polarized light) is typically near zero, as shown in Figure 12c (Schutgens et al., 2004).

Table 4
AirMSPI Viewing Geometry for Smoke Patch Used in Radiative Transfer Calculations

View number	View name	Solar zenith angle (deg)	Solar azimuth angle (deg)	View zenith angle (deg)	View azimuth angle (deg)	Scattering angle (deg)
1	Df	13.76	26.35	68.38	185.09	124.38
2	Cf	13.76	26.35	61.19	186.46	131.63
3	Bf	13.76	26.35	50.19	189.02	142.78
4	Af	13.76	26.35	32.07	195.87	161.28
5	An	13.76	26.35	9.00	259.97	168.94
6	Aa	13.76	26.35	28.32	344.89	140.45
7	Ba	13.76	26.35	47.33	353.38	120.83
8	Ca	13.76	26.35	57.98	356.02	110.01
9	Da	13.76	26.35	65.60	357.54	102.30

Note. AirMSPI = Airborne Multiangle SpectroPolarimetric Imager.

The linearly polarized intensity, Ipol, combines the contributions of the Stokes Q and U components such that

$$\text{Ipol} = \sqrt{Q^2 + U^2}. \tag{9}$$

In this case, the box plots of the Ipol values in Figure 12d essentially represent the absolute values of Q because U is near zero.

Finally, the degree of linear polarization, DoLP, is simply the ratio of the linearly polarized intensity, Ipol, to the intensity, I. The box plots of DoLP shown in Figures 12e and 12f indicate that the degree of linear polarization is somewhat larger for the clear region compared to the smoke region. Initially, this seems counterintuitive as the smoke particles are clearly more polarizing, as shown in Figures 12b and 12d (Q and Ipol, respectively). However, the smoke itself is brighter, which increases the denominator in the calculation of DoLP, reducing the overall value. Figure 12f includes labels for the different AirMSPI views as a function of scattering angle on the plot of DoLP values. The three most oblique aftward views (Da, Ca, Ba) correspond to the smallest scattering angles. The most oblique forward view, Df, has a scattering angle similar to the Ba view. The An and Af views are near a scattering angle of 180° and show very little polarization.

Given the AirMSPI intensity and polarimetric observations shown in Figure 12, we next assess the sensitivity of these observations to the choice of the BC fraction in the smoke aerosol mixture. This is done through full multiple scattering radiative transfer calculations for atmospheres containing a uniformly mixed smoke layer from the surface (taken to be 1 km above sea level) to an altitude of 2.7 km above sea level, which is the height derived for the top of the plume from the AirMSPI observations, with different fractions of BC. All other parameters are fixed based on the in situ observations, with the exception of the AOD and the surface albedo. The successive orders of scatter (SOS) radiative transfer model developed for a coupled atmosphere-ocean system (Zhai et al., 2009, 2010) was used for the calculations, similar to what was done in Kalashnikova et al. (2013). The AOD at 470 nm was varied in the range from 0.17 to 0.51 in increments of 0.01. The surface albedo was assumed to be Lambertian, for simplicity, and was varied in the range from 0.0650 to 0.0975 in increments of 0.0025. Four aerosol mixtures were tested, which correspond to BC fractions of 5%, 10%, 15%, and 20%. The BC refractive indices were taken from Bond and Bergstrom (2006). The viewing geometry used in the radiative transfer calculations is summarized in Table 4.

The sum of the z scores, also called standard scores, was used to assess the agreement between the AirMSPI observations in the smoke plume and the output of the SOS model, similar to what was done in Kalashnikova et al. (2011). A single z score, z_i, for a parameter, f, is calculated as the absolute difference between the observation and the modeled result, normalized by the uncertainty in the observation, σ_i:

$$z_i = \frac{\left| f_{\text{modeled}} - f_{\text{observed}} \right|}{\sigma_i}. \tag{10}$$

As described in greater detail in Kalashnikova et al. (2011), the z scores depend on which observations are used in the comparison, which, in turn, affects the value of σ. The standard deviation of the intensity, σ_I, is directly related to the uncertainty in the radiometric calibration, δ_I, through the relation

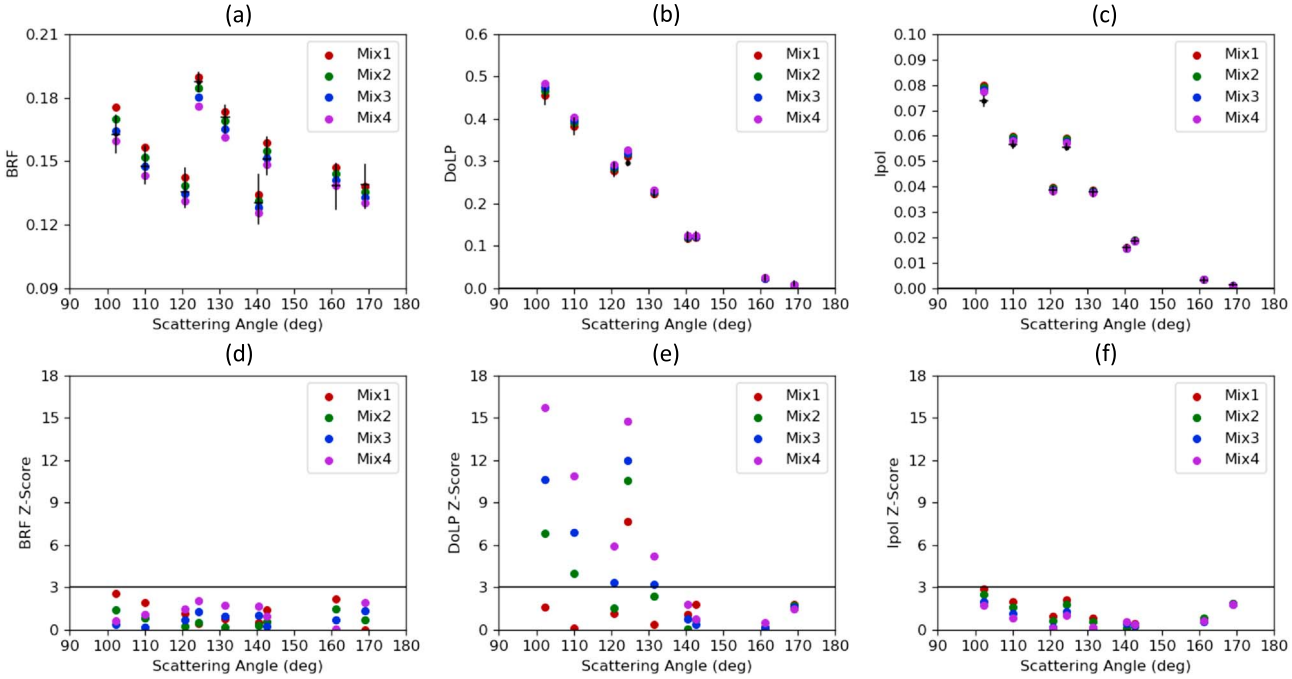

Figure 13. Comparison of Airborne Multiangle SpectroPolarimetric Imager (AirMSPI) observations and successive orders of scatter model results for the best fitting aerosol optical depth and surface albedo at 470 nm. (top row) The box plots represent the variability of the AirMSPI 10 m^2 observations within the 1-km × 1-km smoke patch. The different colors represent the aerosol mixtures containing different fractions of black carbon (5%, 10%, 15%, and 20%). (a) BRF; (b) DoLP; (c) pBRF (Ipol). (bottom row) Sum of *z* scores for each mixture at each scattering angle. The horizontal line shows a distinguishability threshold of 3. (d) BRF; (e) DoLP; (f) pBRF (Ipol).

$$\sigma_I = \delta_I I, \tag{11}$$

We take δ_I for AirMSPI to be approximately 3% at 470 nm, based on vicarious calibration results from previous field campaigns and experience with the MISR instrument on NASA's Terra EOS satellite (Bruegge et al., 2002) (Table 1). It is important to note that the uncertainty in *I*, and therefore BRF, depends on the magnitude of *I* itself. The uncertainty in DoLP, σ_{DoLP}, for AirMSPI has been determined to be less than the requirement of 0.005 (given in Table 1), and we take $\sigma_{\mathrm{DoLP}} = 0.002$ as a typical value based on laboratory comparisons with a polarimetric state generator (Diner et al., 2013). For DoLP the uncertainty is absolute and so does not depend on the magnitude of the DoLP observations. Polarized intensity, Ipol, can be derived from DoLP and *I* and is, therefore, not an independent quantity. This means that the uncertainty in Ipol, σ_{Ipol}, can be determined using the standard approach for the propagation of errors, as discussed in Kalashnikova et al. (2011). The result is

$$\sigma_{\mathrm{Ipol}} = \sqrt{\left(I \cdot \sigma_{\mathrm{DoLP}}\right)^2 + \left(\mathrm{Ipol} \cdot \delta_I\right)^2}. \tag{12}$$

This equation shows that the uncertainty in Ipol depends on the uncertainty in both the DoLP and the intensity. In fact, the uncertainty in the intensity, δ_I, dominates the uncertainty in Ipol for AirMSPI due to the significant difference in the magnitude of δ_I compared to σ_{DoLP} (3% versus 0.2%, respectively). This is to be expected because polarized intensity is actually another measure of intensity, and thus, the uncertainty in Ipol should depend on the radiometric calibration of the instrument.

The sum of the *z* scores for each parameter, BRF, DoLP, and pBRF (Ipol) was examined independently to choose the best solution in the parameter space of AOD, surface albedo, and mixture. A *z* score greater than a specific threshold was taken to represent an unacceptable solution. The minimum threshold that provided a solution in all three parameters, therefore, provided the final result, which was an AOD at 470 nm of 0.33 ± 0.01, a surface albedo at 470 nm of 0.0725 ± 0.0015, and a mixture containing a BC content of 5%. The other mixtures with larger fractions of BC did not provide agreement with the AirMSPI observations within the same *z* score threshold for any combination of AODs or surface albedos. Recall that the MAIAC retrieval from MODIS-Aqua reported an AOD at 470 nm of 0.22 ± 0.03 and a surface reflectance of 0.09 ± 0.02, where the range represents

the spatial standard deviation. As discussed above, the time difference between the AirMSPI and MODIS-Aqua observations was ~50 min, so exact agreement in the AOD would not necessarily be expected. Moreover, the AirMSPI observations were for a patch selected in a dense portion of the plume, which would likely correspond to a larger AOD. The MAIAC surface retrieval is based on an 8-day average and would be less likely to be affected by the presence of smoke. The AirMSPI and MAIAC surface retrievals are in very good agreement, and the BC content is also in good agreement with the SP2 results.

A comparison of the AirMSPI observations and the solutions for the four different BC mixture options is shown in Figure 13. Figures 13a–13c compare the BRF, DoLP, and pBRF (Ipol) results, respectively. The AirMSPI observations are plotted in box plot format, while the SOS results are shown as different-colored dots ranging from Mix1 (5% BC, dark red) to Mix4 (20% BC, purple). Visually, the agreement between the observations and the models is extremely good in all cases. Figures 13d–13f show the *z* scores calculated for each of these comparisons. The horizontal line indicates a *z* score of 3, which was taken in Kalashnikova et al. (2011) to represent the threshold for distinguishability. The actual acceptance threshold for the AirMSPI solution in this case was 2.5, which is slightly lower than the original threshold. The *z* scores for BRF (Figure 13d) show that the mixtures all agree with the AirMSPI observations and are not distinguishable using this metric alone. Similarly, the *z* scores for pBRF (Ipol) (Figure 13f) also show agreement with the AirMSPI observations and even less distinguishability. This is due to the relatively large value of the uncertainty in the AirMSPI observations of intensity, which affects both these metrics in nearly the same way. The uncertainty in AirMSPI observations of DoLP is an order of magnitude smaller, and thus, Figure 13e shows that Mix1 agrees with the AirMSPI observations for all viewing angles, while the other mixtures do not. As mentioned previously, Mix1, with 5% BC, is the only one of the four options that provides agreement with the AirMSPI observations for any choice of AOD and surface albedo within the *z* score threshold.

5. Conclusions

The results in the previous section show how multiangle, spectropolarimetric remote sensing can be used to evaluate the relative contribution of BC particles to the overall aerosol mass in a wildfire smoke plume. This was accomplished through a detailed closure experiment that required extensive use of in situ data provided by the instruments on the CIRPAS Twin Otter aircraft as well as a number of simplifying assumptions. The in situ information was used to constrain the aerosol size distribution and the fractional distribution of components, with the exception of BC, which was allowed to vary in a narrow range from 5% to 20%, consistent with the data from the SP2 and PSAP/nephelometer. The height of the plume was determined by manually tracking a "patch" in the smoke through the sequence of AirMSPI views made from the NASA ER-2 aircraft. The free parameters in the forward radiative transfer model were, therefore, the BC fraction, the AOD, and the surface albedo. The results of a set of radiative transfer runs were compared with the AirMPSI observations in a single polarimetric spectral band (470 nm) taking into account the instrument uncertainties. With these constraints, an AOD of 0.33 ± 0.01, a Lambertian surface albedo of 0.0725 ± 0.0015, and a mixture containing a BC content of 5% were found. Mixtures with larger fractions of BC (10%, 15%, and 20%) did not yield any valid solutions for any combination of AOD or surface albedo. The AOD result is somewhat larger than the MAIAC retrieval from MODIS-Aqua obtained from observations made ~50 min later, but changes in the location and optical depth of the plume limit the utility of such a direct comparison. The surface reflectance, on the other hand, is in very good agreement with the MAIAC retrievals based on an 8-day average of MODIS observations. The BC content is also in good agreement with the SP2 results, which suggests that the BC content and SSA derived from the SP2 data are more trustworthy than the SSA derived from the PSAP/nephelometer data in this case.

The polarimetric sensitivity to BC with an absolute uncertainty of 5% in BC mass fraction for an AOD of 0.33 at 470 nm corresponds to an SSA uncertainty of 0.04 for the refractive indices given by Bond and Bergstrom (2006) and 0.03 for the refractive indices of Hess et al. (1998) (see Figure 9b). This agrees well with known polarimetric sensitivities to SSA over the land (Waquet et al., 2009; Xu et al., 2017). Waquet et al. (2009) demonstrated that an AOD greater than 0.2 at midvisible wavelengths is required to achieve good polarimetric retrieval sensitivity to SSA. The conditions in the Fort Fire case were very close to this limit, and better polarimetric sensitivity to BC may be expected at higher aerosol loadings. The observation viewing geometry could also be a limiting factor, as polarimetric sensitivity depends on instrument viewing conditions (Waquet et al., 2009; Xu et al., 2016). However, the question of retrieval sensitivity was not directly addressed in this study. Further work is needed to better characterize the information contained in the intensity, polarimetric, and multiangle observations.

In terms of the simplifying assumptions, perhaps the one with the greatest influence on the results is the assumption of aerosol external mixing. It is well known that aerosols from wildfires become rapidly coated as they age, which can dramatically change their optical properties (Reid et al., 2005). In addition to acquiring coatings, smoke aerosols can also be highly nonspherical (Chakrabarty et al., 2014), requiring specialized single-scattering techniques beyond the simple Mie calculations used here. While proper treatment of these effects is an active area of research (e.g., Schuster et al., 2016), in this initial study we assume that the magnitude of these effects is small relative to other uncertainties. Additional types of in situ measurements not performed as part of the ImPACT-PM field campaign, such as scanning electron microscopy, would also be required to test more sophisticated approaches.

With 10 m spatial resolution, AirMSPI observations serve as an important bridge between detailed in situ characterization of aerosol plumes and retrievals from future satellite instruments. This work describes an initial step in the direction of satellite characterization of aerosol plume content. Additional coordinated flights and in situ data are needed to more fully evaluate the capability of spectropolarimetric multiangle imaging observations to characterize the aerosol content of atmospheric plumes.

Acknowledgments
We thank three anonymous reviewers for their helpful comments that we believe improved the clarity and readability of this manuscript. Portions of this work were performed at the Jet Propulsion Laboratory, California Institute of Technology, under a contract with the National Aeronautics and Space Administration. The ImPACT-PM flight campaign was funded partially by the JPL President's and Director's Fund (PDF) program, and partially by NASA headquarters. The field data analysis was supported by an Atmospheric Composition Campaign Data Analysis and Modeling (ACCDAM) grant from NASA's Climate and Radiation Research and Analysis Program, under H. Maring. We acknowledge the use of Rapid Response imagery from the Land, Atmosphere Near real-time Capability for EOS (LANCE) system operated by the NASA/GSFC/Earth Science Data and Information System (ESDIS) with funding provided by NASA/HQ. Data sets used in the production of this manuscript are archived at https://eosweb.larc.nasa.gov/project/airmspi/preliminary-datasets/ under the link "Kalashnikova_etal_JGR2018_ImPACT-PM." Access to the data requires a free EarthData login (see webpage for details).

References

Aiken, A. C., DeCarlo, P. F., Kroll, J. H., Worsnop, D. R., Huffman, J. A., Docherty, K. S., et al. (2008). O/C and OM/OC ratios of primary, secondary, and ambient organic aerosols with high-resolution time-of-flight aerosol mass spectrometry. *Environmental Science and Technology*, *42*, 4478–4485. https://doi.org/10.1021/es703009q

Allan, J. D., Deli, A. E., Coe, H., Bower, K. N., Alfarra, M. R., Jimenez, J. L., et al. (2004). A generalised method for the extraction of chemically resolved mass spectra from Aerodyne aerosol mass spectrometer data. *Journal of Aerosol Science*, *35*, 909–922. https://doi.org/10.1016/j.jaerosci.2004.02.007

Baldridge, A. M., Hook, S. J., Grove, C. I., & Rivera, G. (2009). The ASTER spectral library version 2.0. *Remote Sensing of Environment*, *113*, 711–715. https://doi.org/10.1016/j.rse.2008.11.007

Bodhaine, B. A., Wood, N. B., Dutton, E. G., & Slusser, J. R. (1999). On Rayleigh optical depth calculations. *Journal of Atmospheric and Oceanic Technology*, *16*, 1854–1861.

Bond, T. C., & Bergstrom, R. W. (2006). Light absorption by carbonaceous particles: An investigative review. *Aerosol Science and Technology*, *40*(1), 27–67. https://doi.org/10.1080/02786820500421521

Bond, T. C., Doherty, S. J., Fahey, D. W., Forster, P. M., Berntsen, T., DeAngelo, B. J., et al. (2013). Bounding the role of black carbon in the climate system: A scientific assessment. *Journal of Geophysical Research: Atmospheres*, *118*, 5380–5552. https://doi.org/10.1002/jgrd.50171

Bruegge, C. J., Chrien, N. L., Ando, R. R., Diner, D. J., Abdou, W. A., Helmlinger, M. C., et al. (2002). Early validation of the Multi-angle Imaging SpectroRadiometer (MISR) radiometric scale. *IEEE Transactions on Geoscience and Remote Sensing*, *40*(7), 1477–1492. https://doi.org/10.1109/TGRS.2002.801583

Cappa, C. D., Lack, D. A., Burkholder, J. B., & Ravishankara, A. R. (2008). Bias in filter-based aerosol light absorption measurements due to organic aerosol loading: Evidence from laboratory measurements. *Aerosol Science and Technology*, *42*(12), 1022–1032. https://doi.org/10.1080/02786820802389285

Chakrabarty, R. K., Beres, N. D., Moosmuller, H., China, S., Mazzoleni, C., Dubey, M. K., et al. (2014). Soot superaggregates from flaming wildfires and their direct radiative forcing. *Scientific Reports*, *4*, 5508 EP–07. https://doi.org/10.1038/srep05508

Chakrabarty, R. K., Moosmüller, H., Chen, L.-W. A., Lewis, K., Arnott, W. P., Mazzoleni, C., et al. (2010). Brown carbon in tar balls from smoldering biomass combustion. *Atmospheric Chemistry and Physics*, *10*(13), 6363–6370. https://doi.org/10.5194/acp-10-6363-2010

Chow, J. C., Watson, J. G., Lowenthal, D. H., Chen, L.-W. A., & Motallebi, N. (2010). Black and organic carbon emission inventories: Review and application to California. *Journal of the Air & Waste Management Association*, *60*(4), 497–507. https://doi.org/10.3155/1047-3289.60.4.497

DeCarlo, P. F., Kimmel, J. R., Trimborn, A., Northway, M. J., Jayne, J. T., Aiken, A. C., et al. (2006). Field-deployable, high-resolution, time-of-flight aerosol mass spectrometer. *Analytical Chemistry*, *78*(24), 8281–8289. https://doi.org/10.1021/ac061249n

Dennison, P. E., Brewer, S. C., Arnold, J. D., & Moritz, M. A. (2014). Large wildfire trends in the western United States, 1984–2011. *Geophysical Research Letters*, *41*, 2928–2933. https://doi.org/10.1002/2014GL059576

Diner, D. J., Beckert, J. C., Reilly, T. H., Bruegge, C. J., Conel, J. E., Kahn, R. A., et al. (1998). Multi-angle imaging spectroradiometer (MISR) instrument description and experiment overview. *IEEE Transactions on Geoscience and Remote Sensing*, *36*(4), 1072–1087. https://doi.org/10.1109/36.700992

Diner, D. J., Xu, F., Garay, M. J., Martonchik, J. V., Rheingans, B. E., Geier, S., et al. (2013). The Airborne Multiangle SpectroPolarimetric Imager (AirMSPI): A new tool for aerosol and cloud remote sensing. *Atmospheric Measurement Techniques*, *6*(8), 2007–2025. https://doi.org/10.5194/amt-6-2007-2013

Drury, E., Jacob, D. J., Spurr, R. J. D., Wang, J., Shinozuka, Y., Anderson, B. E., et al. (2010). Synthesis of satellite (MODIS), aircraft (ICARTT), and surface (IMPROVE, EPA-AQS, AERONET) aerosol observations over eastern North America to improve MODIS aerosol retrievals and constrain surface aerosol concentrations and sources. *Journal of Geophysical Research*, *115*, D14204. https://doi.org/10.1029/2009JD012629

Dubovik, O., Herman, M., Holdak, A., Lapyonok, T., Tanré, D., Deuzé, J. L., et al. (2011). Statistically optimized inversion algorithm for enhanced retrieval of aerosol properties from spectral multi-angle polarimetric satellite observations. *Atmospheric Measurement Techniques*, *4*(5), 975–1018. https://doi.org/10.5194/amt-4-975-2011

Fuller, K. A., Malm, W. C., & Kreidenweis, S. M. (1999). Effects of mixing on extinction by carbonaceous particles. *Journal of Geophysical Research*, *104*(D13), 15,941–15,954. https://doi.org/10.1029/1998JD100069

Griffin, J. R., & Critchfield, W. B. (1972). The distribution of forest trees in California. In *Pacific Southwest Forest and Range Experiment Station, Forest Service, U.S. Department of Agriculture* (60 pp.).

Hammer, R. B., Stewart, S. I., & Radeloff, V. C. (2009). Demographic trends, the wildland-urban interface, and wildfire management. *Society and Natural Resources*, *22*, 777–782.

Hess, M. P., Koepke, P., & Schult, I. (1998). Optical properties of aerosols and clouds: The software package OPAC. *Bulletin of the American Meteorological Society*, *79*, 831–844.

Holben, B. N., Eck, T. F., Slutsker, I., Tanré, D., Buis, J. P., Setzer, A., et al. (1998). Aeronet—A federated instrument network and data archive for aerosol characterization. *Remote Sensing of Environment*, *66*, 1–16.

Jolleys, M. D., Coe, H., McFiggans, G., McMeeking, G. R., Lee, T., Kreidenweis, S. M., et al. (2014). Organic aerosol emission ratios from the laboratory combustion of biomass fuels. *Journal of Geophysical Research: Atmospheres*, *119*, 12,850–12,871. https://doi.org/10.1002/2014JD021589

Kalashnikova, O. V., Garay, M. J., Davis, A. B., Diner, D. J., & Martonchik, J. V. (2011). Sensitivity of multi-angle photo-polarimetry to vertical layering and mixing of absorbing aerosols: Quantifying measurement uncertainties. *Journal of Quantitative Spectroscopy and Radiative Transfer*, *112*(13), 2149–2163. https://doi.org/10.1016/j.jqsrt.2011.05.010

Kalashnikova, O. V., Garay, M. J., Martonchik, J. V., & Diner, D. J. (2013). MISR Dark Water aerosol retrievals: Operational algorithm sensitivity to particle non-sphericity. *Atmospheric Measurement Techniques*, *6*(8), 2131–2154. https://doi.org/10.5194/amt-6-2131-2013

Kirchstetter, T. W., Novakov, T., & Hobbs, P. V. (2004). Evidence that the spectral dependence of light absorption by aerosols is affected by organic carbon. *Journal of Geophysical Research*, *109*, D21208. https://doi.org/10.1029/2004JD004999

Koepke, P., Hess, M., Schult, I., & Shettle, E. P. (1997). Global aerosol data set (Report N 243). Max-Plank-Institut für Meteorologie, 44.

Kondo, Y., Matsui, H., Moteki, N., Sahu, L., Takegawa, N., Kajino, M., et al. (2011). Emissions of black carbon, organic, and inorganic aerosols from biomass burning in North America and Asia in 2008. *Journal of Geophysical Research*, *116*, D08204. https://doi.org/10.1029/2010JD015152

Kuwata, M., Zorn, S. R., & Martin, S. T. (2012). Using elemental ratios to predict the density of organic material composed of carbon, hydrogen, and oxygen. *Environmental Science & Technology*, *46*(2), 787–794. https://doi.org/10.1021/es202525q

Lack, D. A., Cappa, C. D., Covert, D. S., Baynard, T., Massoli, P., Sierau, B., et al. (2008). Bias in filter-based aerosol light absorption measurements due to organic aerosol loading: Evidence from ambient measurements. *Aerosol Science and Technology*, *42*(12), 1033–1041. https://doi.org/10.1080/02786820802389277

Liu, S., Aiken, A. C., Arata, C., Dubey, M. K., Stockwell, C. E., Yokelson, R. J., et al. (2014). Aerosol single scattering albedo dependence on biomass combustion efficiency: Laboratory and field studies. *Geophysical Research Letters*, *41*, 742–748. https://doi.org/10.1002/2013GL058392

Liu, S., Ahlm, L., Day, D. A., Russell, L. M., Zhao, Y., Gentner, D. R., et al. (2012). Secondary organic aerosol formation from fossil fuel sources contribute majority of summertime organic mass at Bakersfield. *Journal of Geophysical Research*, *117*, D00V26. https://doi.org/10.1029/2012JD018170

Lyapustin, A., Wang, Y., Laszlo, I., Kahn, R., Korkin, S., Remer, L., et al. (2011). Multiangle implementation of atmospheric correction (MAIAC): 2. Aerosol algorithm. *Journal of Geophysical Research*, *116*, D03211. https://doi.org/10.1029/2010JD014986

Martins, J. V., Hobbs, P. V., Weiss, R. E., & Artaxo, P. (1998). Sphericity and morphology of smoke particles from biomass burning in Brazil. *Journal of Geophysical Research*, *103*(D24), 32,051–32,057. https://doi.org/10.1029/98JD01153

Martin, R. V., Jacob, D. J., Yantosca, R. M., Chin, M., & Ginoux, P. (2003). Global and regional decreases in tropospheric oxidants from photochemical effects of aerosols. *Journal of Geophysical Research*, *108*(D3), 4097. https://doi.org/10.1029/2002JD002622

McMeeking, G. R., Fortner, E., Onasch, T. B., Taylor, J. W., Flynn, M., Coe, H., & Kreidenweis, S. M. (2014). Impacts of nonrefractory material on light absorption by aerosols emitted from biomass burning. *Journal of Geophysical Research: Atmospheres*, *119*, 12,272–12,286. https://doi.org/10.1002/2014JD021750

McMeeking, G. R., Kreidenweis, S. M., Baker, S., Carrico, C. M., Chow, J. C., Collett, J. L., et al. (2009). Emissions of trace gases and aerosols during the open combustion of biomass in the laboratory. *Journal of Geophysical Research*, *114*, D19210. https://doi.org/10.1029/2009JD011836

Middlebrook, A. M., Bahreini, R., Jimenez, J. L., & Canagaratna, M. R. (2012). Evaluation of composition-dependent collection efficiencies for the Aerodyne aerosol mass spectrometer using field data. *Aerosol Science and Technology*, *46*(3), 258–271. https://doi.org/10.1080/02786826.2011.620041

Mishchenko, M. I., Dlugach, J. M., Yanovitskij, E. G., & Zakharova, N. T. (1999). Bidirectional reflectance of flat, optically thick particulate layers: An efficient radiative transfer solution and applications to snow and soil surfaces. *Journal of Quantitative Spectroscopy and Radiative Transfer*, *63*(2), 409–432. https://doi.org/10.1016/S0022-4073(99)00028-X

Mok, J., Krotkov, N. A., Arola, A., Torres, O., Jethva, H., Andrade, M., et al. (2016). Impacts of brown carbon from biomass burning on surface UV and ozone photochemistry in the Amazon Basin. *Scientific Reports (Nature Publisher Group)*, *6*, 36940.

Nelson, D. L., Garay, M. J., Kahn, R. A., & Dunst, B. A. (2013). Stereoscopic height and wind retrievals for aerosol plumes with the MISR INteractive eXplorer (MINX). *Remote Sensing*, *5*(9), 4593–4628. https://doi.org/10.3390/rs5094593

Park, K., Kittelson, D. B., Zachariah, M. R., & McMurry, P. H. (2004). Measurement of inherent material density of nanoparticle agglomerates. *Journal of Nanoparticle Research*, *6*(2), 267–272. https://doi.org/10.1023/B:NANO.0000034657.71309.e6

Park, R. J., Jacob, D. J., & Logan, J. A. (2007). Fire and biofuel contributions to annual mean aerosol mass concentrations in the United States. *Atmospheric Environment*, *41*(35), 7389–7400. https://doi.org/10.1016/j.atmosenv.2007.05.061

Pokhrel, R. P., Beamesderfer, E. R., Wagner, N. L., Langridge, J. M., Lack, D. A., Jayarathne, T., et al. (2017). Relative importance of black carbon, brown carbon, and absorption enhancement from clear coatings in biomass burning emissions. *Atmospheric Chemistry and Physics*, *17*(8), 5063–5078. https://doi.org/10.5194/acp-17-5063-2017

Reid, J. S., Eck, T. F., Christopher, S. A., Koppmann, R., Dubovik, O., Eleuterio, D. P., et al. (2005). A review of biomass burning emissions Part III: Intensive optical properties of biomass burning particles. *Atmospheric Chemistry and Physics*, *5*(3), 827–849. https://doi.org/10.5194/acp-5-827-2005

Ryerson, T. B., Andrews, A. E., Angevine, W. M., Bates, T. S., Brock, C. A., Cairns, B., et al. (2013). The 2010 California research at the nexus of air quality and climate change (CalNex) field study. *Journal of Geophysical Research: Atmospheres*, *118*, 5830–5866. https://doi.org/10.1002/jgrd.50331

Sahu, L. K., Kondo, Y., Moteki, N., Takegawa, N., Zhao, Y., Cubison, M. J., et al. (2012). Emission characteristics of black carbon in anthropogenic and biomass burning plumes over California during ARCTAS-CARB 2008. *Journal of Geophysical Research*, *117*, D16302. https://doi.org/10.1029/2011JD017401

Salcedo, D., Onasch, T. B., Dzepina, K., Canagaratna, M. R., Zhang, Q., Huffman, J. A., et al. (2006). Characterization of ambient aerosols in Mexico City during the MCMA-2003 campaign with aerosol mass spectrometry: Results from the CENICA Supersite. *Atmospheric Chemistry and Physics*, *6*(4), 925–946. https://doi.org/10.5194/acp-6-925-2006

Saleh, R., Robinson, E. S., Tkacik, D. S., Ahern, A. T., Liu, S., Aiken, A. C., et al. (2014). Brownness of organics in aerosols from biomass burning linked to their black carbon content. *Nature Geoscience*, *7*(9), 647–650. https://doi.org/10.1038/ngeo2220

Sayer, A. M., Hsu, N. C., Eck, T. F., Smirnov, A., & Holben, B. N. (2014). AERONET-based models of smoke-dominated aerosol near source regions and transported over oceans, and implications for satellite retrievals of aerosol optical depth. *Atmospheric Chemistry and Physics*, *14*(20), 11,493–11,523. https://doi.org/10.5194/acp-14-11493-2014

Schuster, G. L., Dubovik, O., Arola, A., Eck, T. F., & Holben, B. N. (2016). Remote sensing of soot carbon—Part 2: Understanding the absorption ångström exponent. *Atmospheric Chemistry and Physics*, *16*(3), 1587–1602. https://doi.org/10.5194/acp-16-1587-2016

Schutgens, N. A. J., Tilstra, L. G., Stammes, P., & Bréon, F.-M. (2004). On the relationship between Stokes parameters Q and U of atmospheric ultraviolet/visible/near-infrared radiation. *Journal of Geophysical Research*, *109*, D09205. https://doi.org/10.1029/2003JD004081

Schwarz, J. P., Gao, R. S., Spackman, J. R., Watts, L. A., Thomson, D. S., Fahey, D. W., et al. (2008). Measurement of the mixing state, mass, and optical size of individual black carbon particles in urban and biomass burning emissions. *Geophysical Research Letters*, *35*, L13810. https://doi.org/10.1029/2008GL033968

Stier, P., Seinfeld, J. H., Kinne, S., & Boucher, O. (2007). Aerosol absorption and radiative forcing. *Atmospheric Chemistry and Physics*, *7*(19), 5237–5261. https://doi.org/10.5194/acp-7-5237-2007

Taylor, J. W., Allan, J. D., Allen, G., Coe, H., Williams, P. I., Flynn, M. J., et al. (2014). Size-dependent wet removal of black carbon in Canadian biomass burning plumes. *Atmospheric Chemistry and Physics*, *14*(24), 13,755–13,771. https://doi.org/10.5194/acp-14-13755-2014

Urbanski, S. P., Hao, W. M., & Nordgren, B. (2011). The wildland fire emission inventory: Western United States emission estimates and an evaluation of uncertainty. *Atmospheric Chemistry and Physics*, *11*(24), 12,973–13,000. https://doi.org/10.5194/acp-11-12973-2011

Virkkula, A. (2010). Correction of the calibration of the 3-wavelength particle soot absorption photometer (3λ PSAP). *Aerosol Science and Technology*, *44*(8), 706–712. https://doi.org/10.1080/02786826.2010.482110

Wang, J., & Martin, S. T. (2007). Satellite characterization of urban aerosols: Importance of including hygroscopicity and mixing state in the retrieval algorithms. *Journal of Geophysical Research*, *112*, D17203. https://doi.org/10.1029/2006JD008078

Waquet, F., Cairns, B., Knobelspiesse, K., Chowdhary, J., Travis, L. D., Schmid, B., & Mishchenko, M. I. (2009). Polarimetric remote sensing of aerosols over land. *Journal of Geophysical Research*, *114*, D01206. https://doi.org/10.1029/2008JD010619

Watson, J. G. (2002). Visibility: Science and regulation. *Journal of the Air and Waste Management Association*, *52*(6), 628–713. https://doi.org/10.1080/10473289.2002.10470813

Xu, F., Dubovik, O., Zhai, P.-W., Diner, D. J., Kalashnikova, O. V., Seidel, F. C., et al. (2016). Joint retrieval of aerosol and water-leaving radiance from multispectral, multiangular and polarimetric measurements over ocean. *Atmospheric Measurement Techniques*, *9*(7), 2877–2907. https://doi.org/10.5194/amt-9-2877-2016

Xu, F., van Harten, G., Diner, D. J., Kalashnikova, O. V., Seidel, F. C., Bruegge, C. J., & Dubovik, O. (2017). Coupled retrieval of aerosol properties and land surface reflection using the Airborne Multiangle SpectroPolarimetric Imager. *Journal of Geophysical Research: Atmospheres*, *122*, 7004–7026. https://doi.org/10.1002/2017JD026776

Young, D. E., Kim, H., Parworth, C., Zhou, S., Zhang, X., Cappa, C. D., et al. (2016). Influences of emission sources and meteorology on aerosol chemistry in a polluted urban environment: Results from DISCOVER-AQ California. *Atmospheric Chemistry and Physics*, *16*(8), 5427–5451. https://doi.org/10.5194/acp-16-5427-2016

Zhai, P.-W., Hu, Y., Chowdhary, J., Trepte, C. R., Lucker, P. L., & Josset, D. (2010). A vector radiative transfer model for coupled atmosphere and ocean systems with a rough interface. *Journal of Quantitative Spectroscopy and Radiative Transfer*, *111*, 1025–1040. https://doi.org/10.1016/j.jqsrt.2009.12.005

Zhai, P. W., Hu, Y., Trepte, C. R., & Lucker, P. L. (2009). A vector radiative transfer model for coupled atmosphere and ocean systems based on successive order of scatter method. *Optics Express*, *17*, 2057–2079.

Zhang, X., Kim, H., Parworth, C. L., Young, D. E., Zhang, Q., Metcalf, A. R., & Cappa, C. D. (2016). Optical properties of wintertime aerosols from residential wood burning in Fresno, CA: Results from DISCOVER-AQ 2013. *Environmental Science & Technology*, *50*(4), 1681–1690. https://doi.org/10.1021/acs.est.5b04134